The Astrophysical Journal, 997:242 (17pp), 2026 February 1 https://doi.org/10.3847/1538-4357/ae29a9
© 2026. The Author(s). Published by the American Astronomical Society.
OPEN ACCESS

Detection of Stellar Mass Ejections through Extreme Ultraviolet Spectral Lines

Zhixun Cheng[1,2], Anchuan Song[3,4], Guiping Zhou[1,2], Yuming Wang[3,4,5], Hui Tian[6,7], Xiaolei Li[3], Jifeng Liu[2,8], and Jingxiu Wang[2,8]
[1] State Key Laboratory of Solar Activity and Space Weather, National Atronomical Observatories, Chinese Academy of Sciences, Beijing 100101, People's Republic of China; gpzhou@nao.cas.cn
[2] University of Chinese Academy of Sciences, Beijing 100049, People's Republic of China
[3] Deep Space Exploration Laboratory/School of Earth and Space Sciences, University of Science and Technology of China, Hefei 230026, People's Republic of China; ymwang@ustc.edu.cn
[4] CAS Center for Excellence in Comparative Planetology/ CAS Key Laboratory of Geospace Environment, University of Science and Technology of China, Hefei 230026, People's Republic of China
[5] Hefei National Laboratory, University of Science and Technology of China, Hefei 230088, People's Republic of China
[6] School of Earth and Space Sciences, Peking University, Beijing 100871, People's Republic of China
[7] Key laboratory of solar activity and space weather, National Space Science Center, Chinese Academy of Sciences, Beijing 100190, People's Republic of China
[8] National Astronomical Observatories, National Astronomical Observatories, Chinese Academy of Sciences, Beijing 100101, People's Republic of China
Received 2024 September 9; revised 2025 December 2; accepted 2025 December 5; published 2026 January 27

Abstract

Coronal mass ejections (CMEs), since their first observation in 1971, have been widely acknowledged as the most significant eruptive phenomena and the primary cause of catastrophic space weather events within our solar system. Whether similar processes involving stellar mass ejections (SMEs) occur on other stars holds immense potential for advancing our understanding of stellar behavior and providing insights into the search for extraterrestrial life. However, detecting SMEs remains challenging, particularly in establishing reliable approaches and diagnostics. Here, we conduct a proof-of-concept Sun-as-a-star experiment using solar CMEs as proxies, analyzing EUV spectral lines from the Extreme Ultraviolet Variability Experiment on board the Solar Dynamics Observatory. By comparing 26 front-side fast CMEs with 14 confined flares of class M 1.0 and above, we find that the Doppler responses in 18.04, 19.51, and 28.42 nm during CME events provide a promising diagnostic to distinguish Sun-as-a-star CME signals from flare features. We further show that CME characteristics can be reasonably reproduced from the Doppler velocities in these three lines, providing a hopeful diagnostic for inferring otherwise unobservable properties of eruptions on remote stars. These findings advance the exploration and understanding of mass ejections in stars. We therefore advocate the resumption of the EUV observations of extrasolar stars.

Unified Astronomy Thesaurus concepts: Stellar coronal mass ejections (1881); Solar coronal mass ejections (310); Solar flares (1496); Solar extreme ultraviolet emission (1493); Doppler shift (401); Stellar spectral lines (1630)

Materials only available in the online version of record: animations

1. Introduction

Coronal mass ejections (CMEs), as one of the largest explosive phenomena on the Sun, are an efficient way of the Sun to lose mass (W. Mishra et al. 2019) that drives the mass, energy, and magnetic flux flows in the entire heliosphere, and therefore are of importance for the habitability of the Earth system and the existence of a biosphere. Thus, stellar mass ejections (SMEs) are believed to play a similar role in stellar systems and contain the crucial information in understanding the evolution of stars and their circumstellar environments, including the habitability (A. N. Aarnio et al. 2012; J. J. Drake et al. 2013; R. A. Osten & S. J. Wolk 2015; P. Odert et al. 2017).

The significance of solar CMEs was not unveiled until they were first confirmed by coronagraphs in 1971 (J. A. Eddy 1979), about 100 yr after the early detection of solar flares in the 19th century. Likewise, although stellar flares are commonly observed as regular occurrences on stars, the direct confirmation of SMEs has not been attained, despite early indications through the projected velocities surpassing the escape velocities during stellar flares (e.g., E. R. Houdebine et al. 1990; E. W. Guenther & J. P. Emerson 1997). As analogs of CMEs, SMEs have long been believed to be a common physical phenomenon throughout the Universe. Therefore, exploring SME detection through studies of solar CMEs is both valuable and promising.

In previous studies, various observational signatures have been attributed to SMEs. For instance, (M. Leitzinger et al. 2011) analyzed far-ultraviolet line spectra and suggested that an outward Doppler velocity of approximately 84 km s^{-1} during a stellar flare could indicate a possible mass ejection from the stellar corona. C. Argiroffi et al. (2019) employed time-resolved X-ray spectroscopy with the Chandra X-ray Observatory to report a candidate for SME characterized by an upward velocity of 90 ± 30 km s^{-1}, as indicated by the blueshift in the O VIII line. Recent studies have reported probable eruptions of stellar filaments (e.g., K. Namekata et al. 2022, 2024; M. Leitzinger et al. 2024) showing projected bulk velocities. For instance, an outward velocity of 510 km s^{-1} was derived from a blueshifted H_α absorption component (K. Namekata et al. 2022), which closely approaches the escape velocities of the stars.

In a different approach, A. M. Veronig et al. (2021) presented the first study of applying dimming signatures

Original content from this work may be used under the terms of the Creative Commons Attribution 4.0 licence. Any further distribution of this work must maintain attribution to the author(s) and the title of the work, journal citation and DOI.

following a flare in stellar light curves, and proposed indirect evidence of SMEs based on the observations of extreme ultraviolet and X-ray emission. Their results show that solar CME-related dimmings can cause an average decrease in intensity depth of 2.18% over a mean duration of 7.12 hr. In comparison, SME-related dimmings are discussed to cause a much larger intensity decrease of 22.7%, but within a significantly shorter duration of 4.41 hr. These challenging findings—that SME-related dimming is, on average, 10 times deeper than CME-induced dimming yet typically recovers about 3 hr earlier—suggest that stellar corona may differ markedly from the Sun's. Nevertheless, these prior studies have provided valuable insights that an SME could exhibit specific signatures in line-of-sight spectral observations.

It is important to note that identifying and interpreting the Doppler signature of mass motions during solar or stellar eruptions from integrated spectral data is a complex endeavor. Numerous factors require consideration, especially when examining CMEs and SMEs inferred from these signatures. For instance, during solar or stellar eruptions, the simultaneous presence of redshifted and blueshifted components can arise due to the intricate motion of the ejected material. This situation presents a challenge in interpreting Doppler signals, particularly when observing the Sun or stars as integrated sources.

Additionally, solar/stellar eruptive events often feature multiple velocity components corresponding to different stages of the ejection process. Untangling these components is a challenging task essential for determining the true velocities of the material. Furthermore, the motion of the ejected material is frequently intricate, involving rotation, turbulence, and other nonlinear characteristics, which can further obscure the accurate interpretation of Doppler shifts.

Given these complexities, it is crucial to emphasize that extracting reliable velocities from integrated Doppler signatures of CMEs/SMEs demands meticulous consideration of potential sources of error and uncertainty. Although Doppler shifts offer valuable insights into mass motions, interpreting them within the framework of integrated solar/stellar observations remains an active area of research.

In order to ensure that the detected line-of-sight spectral signatures are not originating from other processes, such as chromospheric evaporation during a flare, several questions need to be addressed: (1) Which monitoring spectral line is most suitable for accurately recognizing a CME/SME without mixing effects or ambiguity? This involves considering various factors such as line intensity, line profile, and associated Doppler shift. (2) Can the properties of a CME/SME be quantified through spectral diagnosis? Beyond detecting the presence of a CME/SME, it is important to quantify its properties, such as velocity, mass, and duration. Resolving these questions will establish robust, reliable methods for detecting and characterizing SMEs using spectroscopy. It is an important step toward advancing our understanding of SMEs and their impact on stellar and planetary systems.

2. Data and Methods

2.1. Spectral Observations of SDO/EVE

Thanks to the presence of the Extreme Ultraviolet Variability Experiment (EVE; T. N. Woods et al. 2012) on board the Solar Dynamics Observatory (SDO, W. D. Pesnell et al. 2012), solar CMEs can be utilized to evaluate the detectability of SMEs by considering the Sun as a star. In this work, EVE data from 2012 have been used since EVE works well with most of the spectral lines in this year. During this period, we look up front-side fast CMEs in the CME catalog[9], and identify a total of 26 front-side fast CMEs (see Table 1) that have a projected velocity 800 km s^{-1} and are associated with a C-class or stronger flare within 85° in both longitude and latitude based on the criteria defined in our previous studies (Y. M. Wang et al. 2002; G. Zhou et al. 2003).

SDO/EVE provides measurements of full-disk solar EUV irradiance, treating the Sun as a star, across a wavelength range of 5–105 nm. The primary instrument of EVE is the Multiple EUV Grating Spectrograph (MEGS), which consists of two spectrographs: MEGS-A (5–37 nm) and MEGS-B (350–1050 nm). MEGS-A has a spectral resolution of 0.1 nm and a cadence of 10 s.

In this work, we focus on MEGS-A spectra to investigate CME dynamics for two main reasons. First, MEGS-A provides continuous Sun-as-a-star coverage, enabling reliable detection of front-side CMEs, whereas MEGS-B observes intermittently —typically 5 minutes hr^{-1}—so most CME events are missed. Second, CMEs are commonly associated with high-temperature signatures, such as flux-rope eruptions, which can be well captured by MEGS-A; by contrast, MEGS-B is more sensitive to lower-temperature processes in the transition region and chromosphere. For these reasons, we primarily analyze MEGS-A data to probe CME dynamics.

To identify the preferred spectral lines for detecting CMEs, we analyze 13 EUV spectral lines (Fe XVIII 9.39 nm, Fe VIII 13.09 nm, Fe XX 13.29 nm, Fe IX 17.11 nm, Fe X 17.72 nm, Fe XI 18.04 nm, Fe XII 19.51 nm, Fe XIII 20.20 nm, Fe XIV 21.13 nm, Fe XV 28.42 nm, Fe XVI 33.54 nm, Fe XVI 36.08 nm and Mg IX 36.81 nm) corresponding to the CME favorable temperature ranging from 0.1 to 10 MK. The temperature response of these solar emission lines is obtained with the aid of the atomic database provided by CHIANTI (version 6.0.1, K. P. Dere et al. 1997, 2009), which allows us to simulate the behavior of solar emission lines using an isothermal model.

The main procedure used for this purpose is "CH_SYNTHETIC.PRO" from the CHIANTI package, which can be accessed at this URL: http://www.lmsal.com/solarsoft/. When running the CHIANTI procedure, we match the solar corona with elemental abundances and define CME-related active regions based on Differential Emission Measure (DEM) distributions as we did before (Y. Wang et al. 2016). The simulations give us the temperature response of each line, including irradiance contributions, typical temperatures, and central wavelength of the target line, as well as its neighboring lines. One can refer to Figure 1 for examples illustrating these properties.

Two criteria are further utilized to select the target lines for CME detection. The first criterion is that the spectral line is not heavily contaminated by neighboring lines within its dominant temperature range. For instance, let us consider the spectral line Fe XVI 36.08 nm, which primarily corresponds to temperatures between $6.2 < \log T < 7.0$. In this temperature range, the neighboring spectral line of Mn XV 36.10 nm might significantly overlap with Fe XVI 36.08 nm, resulting in a

[9] https://cdaw.gsfc.nasa.gov/CME_list/index.html

Table 1
Front-side Fast CMEs in 2012

No.	Rem.	Date	Flare (UT)			LASCO/CMEs		GCS/CMEs				Max. V_d (km s^{-1})		
			Start-Peak-End	Class	Loc.	First App. in C2 (UT)	Lin. Vel. (km s^{-1})	Face-on Wid. (deg)	Edge-on Wid. (deg)	Prop. Dir.	Vel. (km s^{-1})	28.42 nm	19.51 nm	18.04 nm
1		2012/01/19	13:44-16:05-17:50	M3.2	N30E27	14:36:05	1120	142	70	N43E17	1090	-67.2 ± 2.6	108.3 ± 15.4	117.4 ± 17.0
2	Contam.	2012/01/23	03:38-03:59-04:34	M8.7	N29W23	04:00:05	2175	193	61	N41W16	1906	-111.4 ± 16.8	-125.1 ± 26.1	-98.3 ± 21.1
3		2012/01/26	03:58-05:42-07:03	C6.4	N26W60	04:36:05	1194	85	45	N56W71	1033	-42.1 ± 1.9	-102.4 ± 11.3	-112.0 ± 18.6
4		2012/01/27	17:37-18:37-18:56	X1.7	N29W72	18:27:52	2508	179	119	N27W78	1807	-27.1 ± 3.9	-298.5 ± 15.9	-292.3 ± 16.6
5	Contam.	2012/03/03	18:13-19:48-20:46	C1.9	N17E73	18:36:05	1078	76	54	N22E61	982	31.6 ± 5.2	39.8 ± 9.2	23.7 ± 7.9
6		2012/03/04	10:29-10:52-12:16	M2.0	N18E68	11:00:07	1306	150	43	N27E41	1190	-35.7 ± 6.9	22.3 ± 16.3	17.7 ± 12.4
7	Contam.	2012/03/07	00:02-00:24-00:40	X5.4	N17E29	00:24:06	2684	140	58	N33E36	2012	-97.1 ± 13.3	60.4 ± 29.8	46.4 ± 17.7
8	Contam.	2012/03/07	01:05-01:14-01:23	X1.3	N19E13	01:30:24	1825	263	122	N09E03	1922	-97.4 ± 19.8	155.1 ± 34.7	101.3 ± 25.6
9		2012/03/09	03:22-03:53-04:18	M6.3	N17E01	04:26:09	950	73	37	N06W01	1188	-117.7 ± 18.0	124.8 ± 24.1	101.9 ± 16.3
10		2012/03/10	17:15-17:44-18:30	M8.4	N18W13	18:00:05	1296	107	44	N18W16	1271	-87.5 ± 12.2	31.5 ± 23.2	-16.3 ± 20.0
11		2012/03/27	02:50-03:08-03:22	C5.3	N21W04	03:12:09	1148	40	24	N35W13	1083	-68.2 ± 13.2	21.1 ± 14.7	-33.6 ± 10.9
12		2012/04/05	20:49-21:10-21:57	C1.5	N17W19	21:25:07	828	115	64	N21W29	835	-55.9 ± 8.2	-69.5 ± 19.0	-67.5 ± 18.0
13		2012/04/09	12:12-12:44-13:08	C3.9	N20W52	12:36:07	921	94	34	N12W40	892	69.5 ± 5.8	-124.7 ± 12.8	-130.9 ± 23.4
14		2012/04/30	06:56-07:38-08:19	C3.9	S18W80	07:48:05	992	47	26	S26W86	969	45.0 ± 4.7	-228.8 ± 17.8	-255.3 ± 18.3
15		2012/05/17	01:25-01:47-02:14	M5.1	N13W73	01:48:05	1582	144	72	S09W81	1451	156.4 ± 14.9	-183.6 ± 26.1	-240.2 ± 31.7
16		2012/06/02	04:15-04:31-04:55	C1.5	N14E49	04:36:05	1175	58	35	N24E44	1347	-99.3 ± 13.0	-10.4 ± 11.3	-26.2 ± 15.9
17	Contam.	2012/06/05	20:49-20:59-21:09	C4.2	N15E34	21:33:05	824	76	18	N11W03	1487	75.9 ± 8.3	138.7 ± 15.4	93.1 ± 11.1
18	Contam.	2012/06/13	11:29-13:17-14:31	M1.2	S17E28	14:36:05	1153	76	51	S31E14	802	-159.2 ± 4.7	-144.4 ± 14.3	-160.4 ± 10.2
19		2012/06/14	12:52-14:35-15:56	M1.9	S17E14	14:12:07	987	178	125	S23W03	1227	-149.2 ± 8.0	87.8 ± 15.3	64.4 ± 9.1
20		2012/06/28	19:38-19:42-20:16	C1.7	N15E58	20:00:05	1313	82	49	N43E60	1390	-22.6 ± 7.7	139.2 ± 10.9	127.7 ± 9.1
21	Contam.	2012/07/05	21:37-21:45-21:51	M1.6	S17W23	22:00:04	980	54	28	S34W70	1064	132.2 ± 18.0	187.5 ± 14.1	189.3 ± 22.4
22	Contam.	2012/07/08	16:23-16:32-16:42	M6.9	S17W63	16:36:07	1572	92	45	S32W92	1644	-227.0 ± 6.2	-272.0 ± 29.3	-277.9 ± 26.1
23		2012/07/12	15:37-16:49-17:30	X1.4	S17E06	16:48:05	885	82	77	S10W04	1341	-103.6 ± 11.4	-161.1 ± 10.0	-197.8 ± 16.2
24	Contam.	2012/08/04	11:04-15:00-16:49	C3.5	S23E45	13:36:23	856	83	62	S16E47	796	-158.5 ± 4.9	75.1 ± 11.6	59.2 ± 9.8
25		2012/08/31	19:45-20:43-21:51	C8.4	S16E56	20:00:05	1442	83	42	S04E31	1290	-34.3 ± 16.5	98.9 ± 25.2	99.0 ± 26.3
26	Contam.	2012/11/13	01:58-02:04-02:06	M8.6	S22E43	02:24:06	851	26	13	S41E56	832	-34.2 ± 7.4	-32.1 ± 11.1	-14.0 ± 12.0

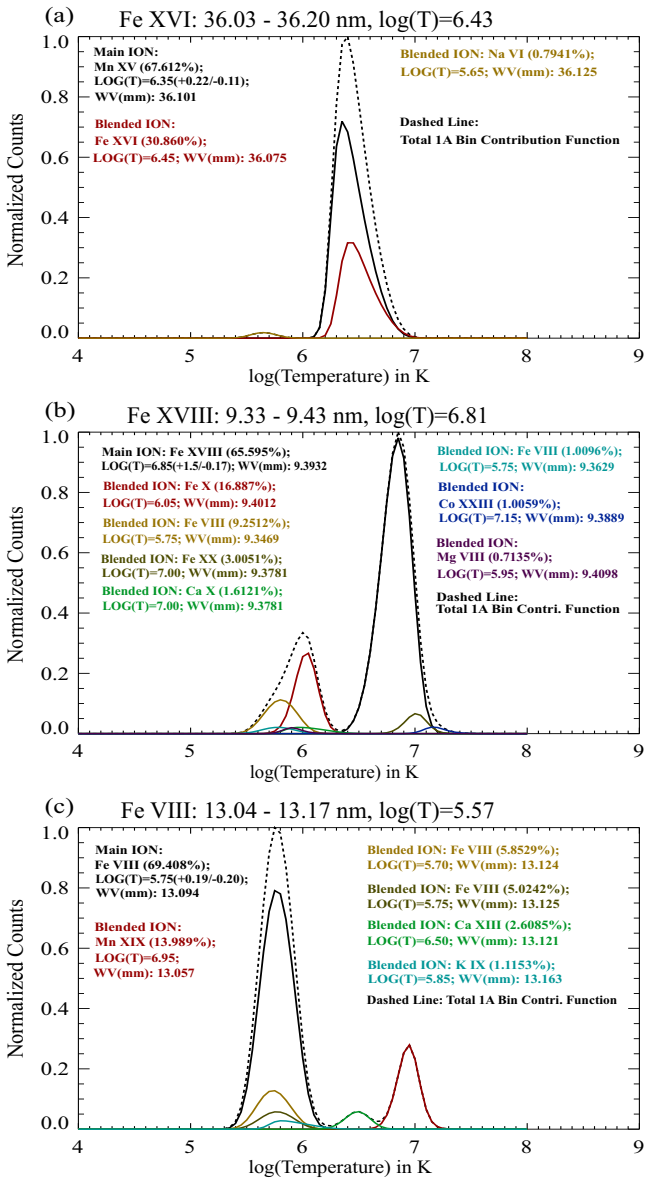

Figure 1. The temperature response curves of three spectral lines, Fe XVI 36.08 nm (a), Fe XVIII 9.39 nm (b), and Fe VIII 13.09 nm (c), derived from the CHIANTI atomic database. In each panel, the percentages indicated in parentheses represent the contributions of different ions to the total emission from neighboring wavelengths. The temperatures associated with these ions, along with their respective uncertainties, are determined based on the full width at half-maximum of the corresponding peak emission.

substantial blending effect. This blending can contribute up to 68% of the total irradiance, as illustrated in Figure 1(a). Such a high level of mixing makes it extremely challenging to accurately determine the temporal variations of the monitoring line. Consequently, Fe XVI 36.08 nm is excluded from the selection process due to this severe contamination by Mn XV 36.10 nm. Similarly, the spectral lines Fe XX 13.29 nm and Mg IX 36.81 nm are also excluded for the same reason.

The second criterion is that the line will not be replaced by neighboring lines due to temperature changes. For instance, considering the hot coronal line Fe XVIII 9.39 nm, which exhibits optimal response temperatures between $6.3 < \log T < 7.2$, as depicted in Figure 1(b). However, during the process where the temperature falls below $\log T = 6.3$, Fe XVIII 9.39 nm will be replaced by Fe X 9.40 nm and/or Fe VIII 9.35 nm, which is only 0.01 or 0.04 nm away from the target line at 9.39 nm. Such a substitution of the target line is often inconspicuous and may cause a fake Doppler velocity of about 320 or 1280 km s^{-1}. Similarly, a colder spectral line can also be readily replaced by a neighboring hotter line, as demonstrated in Figure 1(c). Considering the line of Fe VIII 13.09 nm, which has optimal response temperatures between $5.3 < \log T < 6.2$. This line may be substituted by lines such as Ca XIII 13.12 nm or Mn XIX 13.06 nm when the erupting temperature ($\log T$) exceeds 6.2. As per this second criterion, seven spectral lines are excluded from the selection process: Fe XVIII 9.39 nm, Fe VIII 13.09 nm, Fe IX 17.11 nm, Fe X 17.72 nm, Fe XIII 20.20 nm, Fe XIV 21.13 nm, and Fe XVI 33.54 nm.

Based on the satisfaction of the two criteria described above, the selection process has resulted in three remaining spectral lines suitable for monitoring the CME process. These lines are Fe XI 18.04 nm, Fe XII 19.51 nm, and Fe XV 28.42 nm. Their respective peak response temperatures are 6.07, 6.13, and 6.30 in $\log T$, and they are more sensitive to the plasma motion of CMEs than flares (Z. Cheng et al. 2019). Compared to other lines in the EVE dataset, these three lines exhibit relatively lower levels of contamination by neighboring lines and are suitable for the study here.

2.2. Doppler Velocity Derived from the EVE Spectral Lines

As illustrated in Figure 2, we first get the irradiance variation (represented by the blue diamonds) at any given moment by subtracting the preflare irradiance (average over 2 hr ahead of the eruption, represented by the black diamonds) from the observed irradiance at each wavelength. Then we determine the difference between the peak wavelengths of the irradiance variation (blue) and the preflare average irradiance (black) by using spline interpolations, as shown by the two corresponding curves in the figure. The Doppler velocity is calculated as:

$$v_{\rm d} = 3 \times 10^5 \, \frac{w_{\rm c1} - w_{\rm c2}}{w_{\rm c2}} \ {\rm km\ s^{-1}},$$

where: $v_{\rm d}$ represents the Doppler velocity, $w_{\rm c1}$ is the peak wavelength of the irradiance variation profile (blue), and $w_{\rm c2}$ is the peak wavelength of the preflare profile (black). The uncertainty in $v_{\rm d}$ is identified as the 3σ standard deviation of the fluctuated Doppler velocity within the 2 hr before the flare. By applying the method, the Doppler velocity as well as its temporal evolution with a cadence of 10 s can be deduced.

Previous studies had shown that the CME propagation speed rises consistently with the soft X-ray flux of the associated flare, and reaches the maximum at the flare peak, after which the CME speed remains unchanged or goes down (e.g., J. Zhang et al. 2001; P. T. Gallagher et al. 2003; J. Qiu et al. 2004). According to this picture, the Doppler velocity caused by a CME should be most significant around the flux peak of the associated flare and form a local maximum or minimum. Thus, we search for the local maximum/minimum (either positive or negative) Doppler velocity appearing closest to the flare peak time within the time window from the flare onset until 2 hr after the flare peak time, and assign the maximum or minimum Doppler velocity to the event as the representative value listed in Table 1. Occasionally, Doppler velocity shows a monotonous changing profile with a local maximum/minimum in the time window. For such a case, we simply choose the value of the Doppler velocity at 2 hr after the flare peak time. As mentioned in the main text, there are also some events contaminated with other comparable flares or CMEs within the

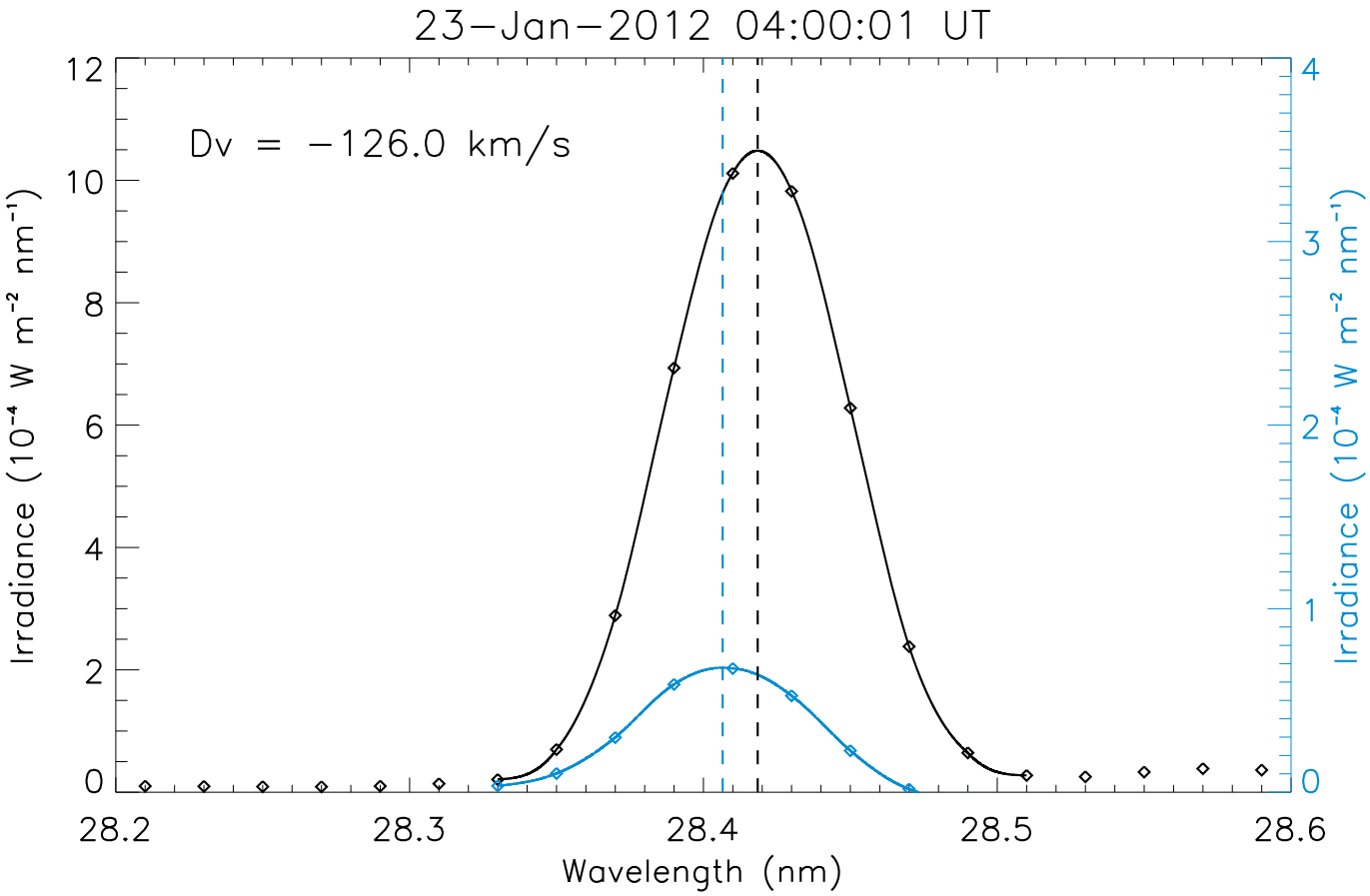

Figure 2. The irradiance profiles for the spectral line Fe XV 28.42 nm, depicted at 04:00 UT during the CME event on 2012 January 23. The black diamonds indicate the average irradiance within 2 hr ahead of the CME initiation, and the blue ones, scaled by the *y*-axis on the right-hand side, represent the irradiance variation at the moment of interest. The black and blue curves are two spline interpolations to the corresponding data points, of which the peaks are denoted by dashed lines.

2 hr interval. The searching will stop at the onset of the next flare or CME. All the events could be found in the file "The plots of all the 26 CMEs.pptx" at https://nadc.china-vo.org/res/r101384/ or doi:10.12149/101384.

2.3. 3D Information of the CMEs by GCS Modeling

A CME is considered the flux-rope structure. Therefore, we use the Graduated Cylindrical Shell (GCS) forward modeling (A. F. R. Thernisien et al. 2006; A. Thernisien 2011) to derive the 3D parameters of a CME from the observations from three perspectives: SOHO-LASCO C2/C3 and STEREO-A/B-SECCHI COR2. The GCS modeling involves several geometric parameters. These parameters include the longitude (ϕ) and latitude (λ) in Heliocentric Earth Equatorial coordinates, the height (H) of the CME's leading edge, the tilt angle (γ) and half-angle (σ) of the flux-rope axis, and the aspect ratio (κ), which represents the sine of the cone half-angle at the flux-rope foot. The longitude and latitude provide information about the CME's propagation direction. The flux-rope model of the CME is constructed by fitting the CME fronts observed in different coronagraph images, as depicted in Figure 3. By employing linear fitting of the CME front height (H) at different times, the CME deprojected front velocity (v) can be derived. The CME angular width adopted in the correlation analysis below is the mean value of the face-on width and the edge-on width listed in Table 1.

2.4. Correlation Analysis

The Doppler responses of CMEs are probably attributed to the mix of multiple influence factors, e.g., the motion of the flaring and dimming plasmas in the source region and the motion of the CME plasma. We investigate six factors f_1–f_6, which denote flare classes, flare locations, propagation directions, CME projection speeds, deprojected speeds, and CME angular widths, respectively. The first three factors f_1–f_3 are obtained from the CME catalog, and the other factors f_4–f_6 are derived from the coronagraphic images with the aid of the GCS model. To find the contribution of each factor to the observed Doppler responses, we use the multivariable regression method with the function of $v_{\rm Doppler} = c_0 + \sum_{i=1}^{6} c_i f_{i,\rm norm}^{n_i}$. It should be noted that the values of flare location and CME propagation direction, f_2 and f_3, are the angles away from the Sun–Earth line converted from their longitudes and latitudes. Since the factors are not in the same physical units, we normalize the value of each factor, f_i, into a reasonable range. The flare class is normalized as $f_{1,\rm norm} = \frac{f_1}{f_{x_{10}}}$, in which $f_{x_{10}}$ is the soft X-ray intensity of a X10-class flare, the directions, f_2 and f_3, are normalized as $f_{i,\rm norm} = \frac{f_i - 90^\circ}{90^\circ}$, the velocities, f_4 and f_5, are normalized as $f_{i,\rm norm} = \frac{f_i}{3000\ \rm km\ s^{-1}}$, and the angular width, f_6, as $f_{6,\rm norm} = \frac{f_6}{180^\circ}$. Except that the factors of directions fall into a range of $[-1,1]$, the other factors in a range of $[0,1]$. The order of each factor, n_i, is an integral

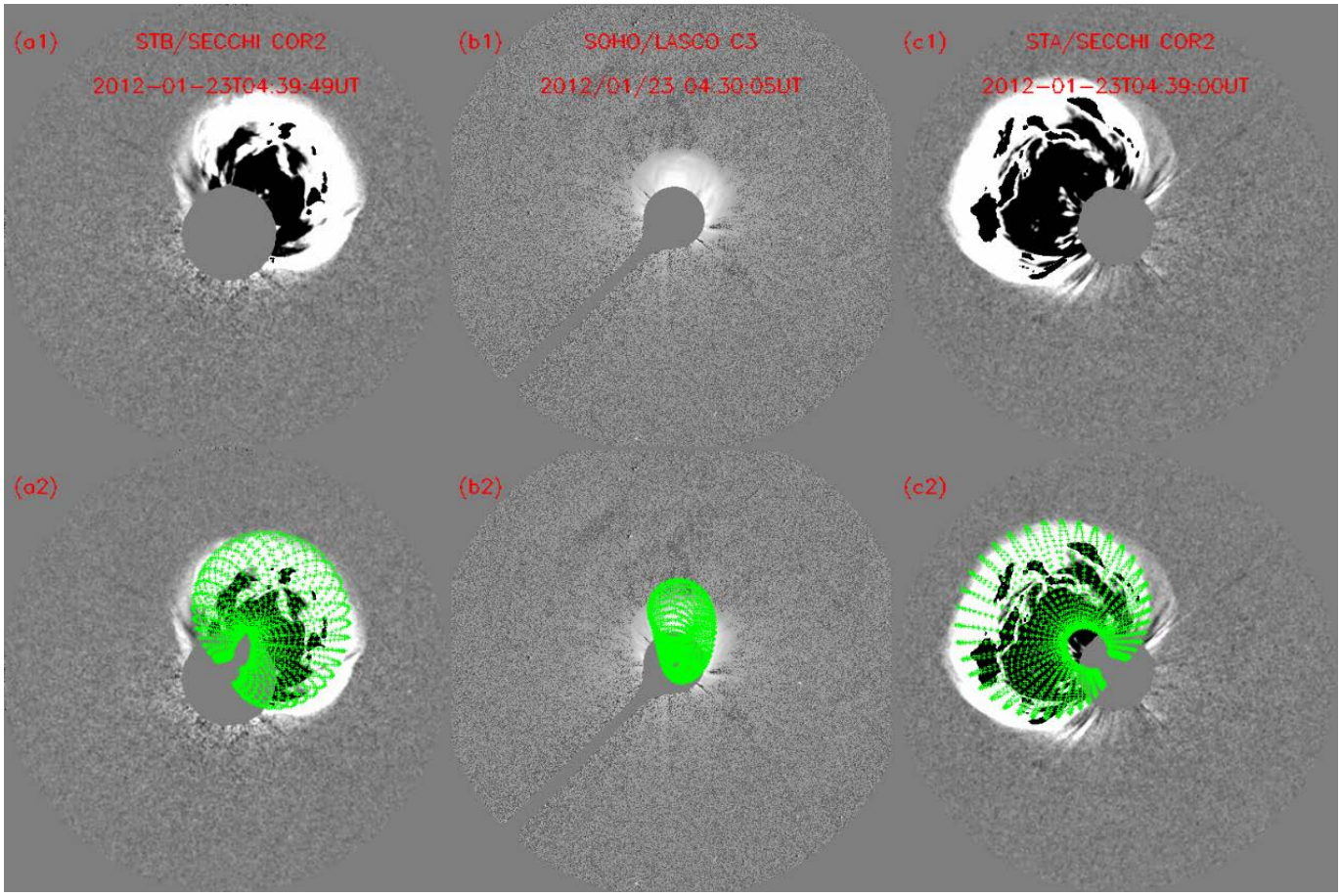

Figure 3. The GCS modeling results for the CME event occurring on 2012 January 23. Panels (a1) to (c1) depict the coronagraph images capturing the CME structure observed from SOHO-LASCO C2/C3 and STEREO-A/B-SECCHI COR2 at 04:30 UT and 04:40 UT, respectively. To represent the CME fronts derived from the GCS model, panels (a2) to (c2) illustrate green surfaces. These surfaces indicate the shape and position of the CME fronts as determined by the GCS modeling technique. The GCS model takes into account the available observational data and simulates the 3D structure of the CME. By comparing the model-derived CME fronts with the actual coronagraph images, we can assess the accuracy of the GCS model and gain insights into the spatial and temporal evolution of the CME during the observed time interval.

varying from 0 to 3 to see at which order the best fitting can be obtained. We do not try a higher order, because a higher even/odd order has no fundamental difference in physics from the lower even/odd order, and a higher order may increase the possibility of false high correlation. The contribution of each factor is evaluated by $\frac{|c_i f_{i,\mathrm{norm}}^{n_i}|}{|c_0|+\sum_{i=1}^{6}|c_i f_{i,\mathrm{norm}}^{n_i}|}$.

The best-fit is obtained when the overall difference (or residual velocity) between the modeled and measured Doppler velocity is minimized. The confidence level (*cl*) is evaluated by the following procedure. We randomize the factors and Doppler velocities in their own ranges bounded by their maximum and minimum values, and apply the above multi-variable regression to obtain the highest correlation coefficient (*cc*). Then, by repeating this step 1000 times, we count how many times (*N*) we get a worse result. The value of *cl* is just $N/1000$ with 100% meaning the highest confidence.

3. Observations and Results

3.1. Doppler Signatures of Front-side Fast CMEs

As an example, Figure 4 shows a fast CME occurring on 2012 July 12. A partial halo CME associated with an X1.4 flare at the source location of S17°E06° can be clearly seen in the southwest direction in the coronagraphic image. The CME propagated with a projected speed in the plane of the sky up to 885 km s^{-1}. The light curves of the three specific lines and the soft X-ray are shown in the right panels of the figure, as well as the calculated Doppler velocities. It can be found that the intensities of the soft X-ray and the hottest line, 28.42 nm, show significant enhancements during the eruption, whereas the other two lines decrease weakly. All three lines exhibit blueshifted Doppler velocities that can reach a maximum of −100 to −200 km s^{-1} during the main phase and recovering phase of the flare.

All the 26 fast CME events were accompanied with either negative or positive Doppler velocity, i.e., either blue or red Doppler shift, in the three lines. The representative Doppler velocities associated with each event have been listed in Table 1. The plots of all the other 25 events could be found at the website https://nadc.china-vo.org/res/r101384/ or doi:10.12149/101384. It should be noted that not all the 26 events are so clear, and we find that 10 events are contaminated by other comparable flares or CMEs before we can find a clear Doppler velocity peak, as indicated in Table 1 and the online plots. The upper panels of Figures 5(a)–(c) show the distributions of the maximum Doppler velocities for the 26 events, which range from about −300 to 200 km s^{-1}. If we only look at the 16 clear events, the range of the maximum Doppler velocity has no fundamental difference except for 28.42 nm, of which the range narrows down to about −150 to 200 km s^{-1}. Considering the uncertainty in estimating the Doppler

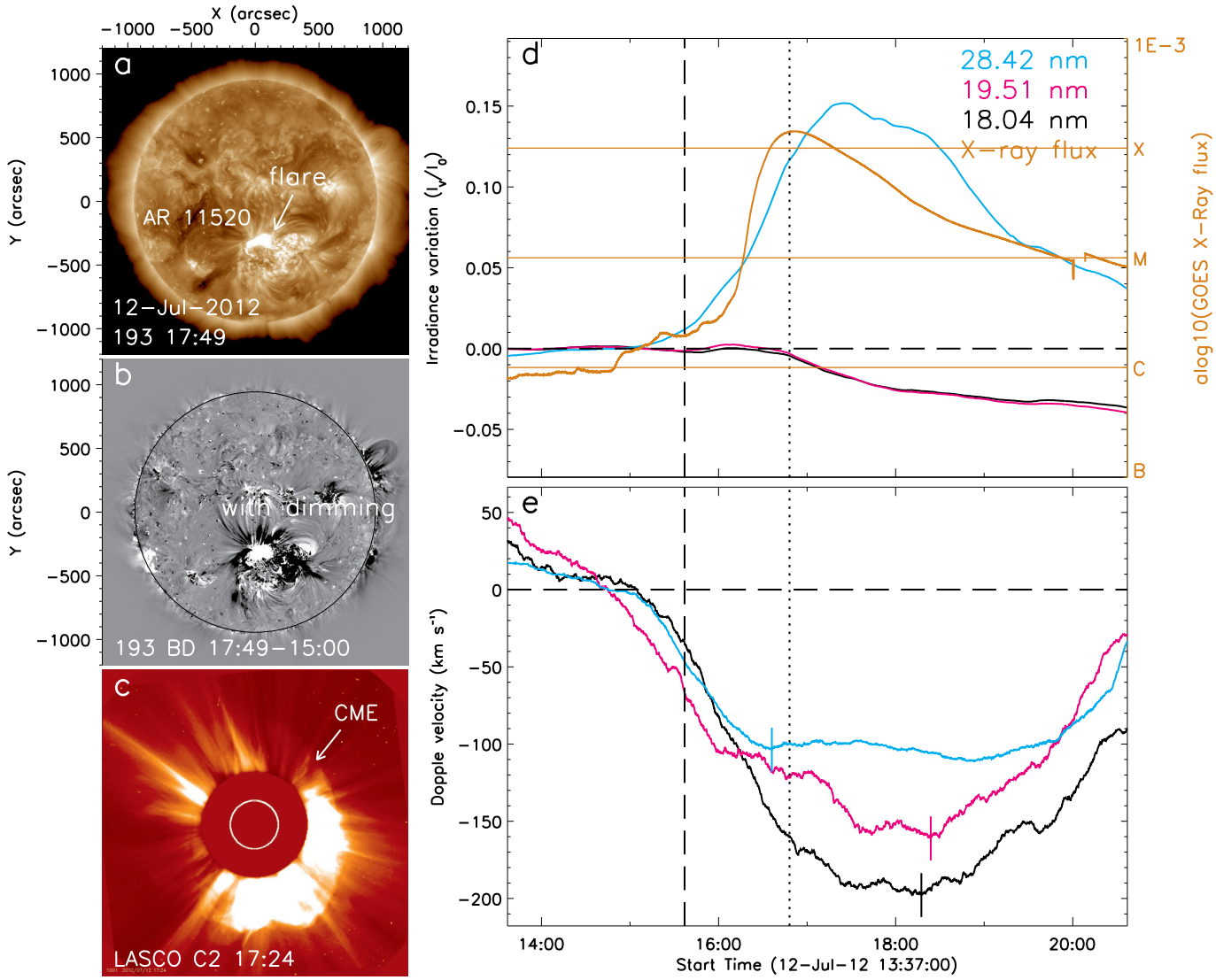

Figure 4. The CME that occurred on 2012 July 12 exemplifies the negative Doppler velocity (blueshift) observed in CMEs propagating toward Earth. The initiation of this CME can be seen in the SDO/Atmospheric Imaging Assembly 19.3 nm image taken at 17:24 UT (Figure 4(a)). It originated in NOAA Active Region 11520 and was associated with an X1.4 flare. The base-difference image at 19.3 nm (Figure 4(b)), obtained by subtracting a pre-event image at 15:00 UT from the one at 17:24 UT, illustrates the simultaneous occurrence of coronal dimming along with the CME. In the image (Figure 4(c)) at 17:24 UT from the C2 instrument on board the SOHO/LASCO, the propagation of this CME is captured. In Figure 4(d), the soft X-ray flux emission from the Geostationary Operational Environmental Satellite (GOES) is represented by the orange color, with the *y*-axis on the right side. The Sun-as-a-star light curves from the SDO/EVE instrument are presented in three passbands: 28.42 nm (blue color), 19.51 nm (purple color), and 18.04 nm (black color). The irradiance variation at each moment is divided by the average value within 2 hr before the eruptive initiation. The horizontal dashed line indicates 0% relative irradiance difference. Based on the Doppler shifts observed in the spectral lines of SDO/EVE, negative Doppler velocities corresponding to the blueshifts are deduced in all three passbands (Figure 4(e)), where the vertical bars indicate the identified maximum Doppler velocities associated with the CME. The vertical dashed and dotted lines mark the initial moments of the related flare and the first appearance of the CME in Large Angle and Spectrometric Coronagraph/C2, respectively.

(An animation of this figure is available in the online article.)

velocity that is typically less than 30 km s^{-1}, we find that the Doppler signatures for these fast CMEs are significant. To obtain the most reliable results, in the following main text, we show the analysis results of the 16 clear events if not specified.

3.2. Doppler Signatures of Confined Flares

On the other hand, another group consisting of 14 confined flares (e.g., Z. Svestka & E. W. Cliver 1992; J. Feynman & A. J. Hundhausen 1994; L.M. Green et al. 2002) with intensities greater than M1.0 class (see Table 2) is built for comparison. Among them, eight events occurred in 2012, and the other six were selected from 2011 and 2013 to increase the sample size. Unlike powerful and eruptive flares, a confined flare does not result in the ejection of a significant amount of solar material into space that could be recorded in the CME catalog. Instead, they release a burst of energy in the form of intense electromagnetic radiation, including X-rays and ultraviolet light. The similar analysis of Doppler response has been conducted on the 14 confined flares, of which six events were also included in the sample studied by A. M. Veronig et al. (2021). We find that the maximum Doppler velocities associated with these events are scattered in a range of about −160 to 130 km s^{-1}, obviously narrower than that for the front-side fast CMEs (see the colored histograms in Figures 5(a)–(c)).

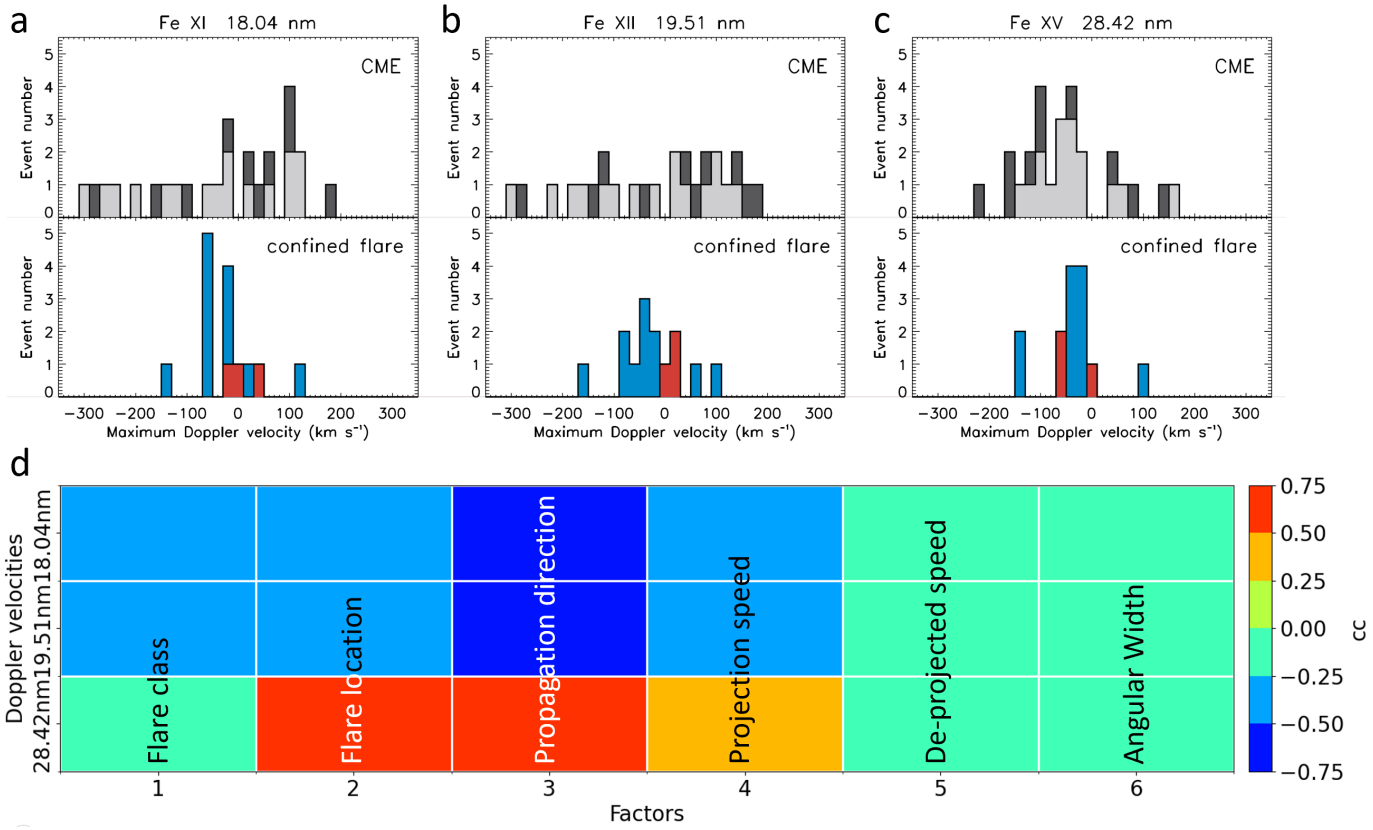

Figure 5. The distributions of maximum Doppler velocities and the correlations between factors and the maximum Doppler velocities. (a)–(c) The distributions of the 26 CME events (with the 10 contaminated in dark, upper panels) and 14 confined flares (with the three pure confined in red, lower panels). Their maximum Doppler velocities are sorted and grouped into bins with a size of 20 km s^{-1}. The three pure-confined flares without any identifiable mass motions are shown in red. (d) The map of the correlations between six factors (horizontal axis) and the maximum Doppler velocities in the three lines (vertical axis), with the value of the Pearson correlation coefficient (*cc*) associated with each grid indicated by the color bar on the right side.

Table 2
Lists of Confined Flare and Pseudoconfined Ones

No.	Rem.	Date	Flare (UT)			Max. V_d (km s^{-1})		
			Start-Peak-End	Class	Location	28.42 nm	19.51 nm	18.04 nm
1	Contaminated by a neighbor ejection	2011/03/09	23:13-23:23-23:29	X1.5	N09E55	-141.5 ± 35.0	-33.2 ± 37.8	-10.6 ± 20.8
2	Pure confined	2011/04/22	15:47-15:53-16:11	M1.2	S17E43	-54.6 ± 11.8	18.2 ± 16.0	-8.0 ± 13.6
3	Pure confined	2011/07/30	02:04-02:09-02:12	M9.3	N16E33	-65.4 ± 7.9	27.5 ± 13.1	37.5 ± 8.1
4	Pure confined	2011/11/05	20:31-20:38-20:54	M1.8	N19E45	6.0 ± 2.9	8.4 ± 15.8	-11.9 ± 9.2
5	Pseudoconfined	2012/02/06	19:31-20:00-20:17	M1.0	N19W60	109.8 ± 6.9	67.8 ± 14.6	17.8 ± 10.6
6	Pseudoconfined	2012/03/17	20:32-20:39-20:42	M1.4	S20W25	-40.5 ± 9.0	-152.5 ± 5.9	-140.2 ± 15.6
7	Contaminated by a back CME	2012/05/08	13:02-13:08-13:12	M1.4	N14E43	-20.3 ± 5.2	-38.0 ± 9.7	-58.2 ± 6.6
8	Failed ejection	2012/05/09	12:21-12:32-12:36	M4.7	N13E31	-10.9 ± 7.1	-25.5 ± 16.0	-19.6 ± 15.3
9	Failed ejection	2012/05/09	14:02-14:08-14:14	M1.8	N06E22	-21.8 ± 17.8	-18.0 ± 15.0	-25.4 ± 21.6
10	Failed eruption	2012/05/10	04:11-04:18-04:23	M5.7	N12E22	-47.7 ± 9.6	-39.4 ± 12.8	-56.9 ± 10.4
11	Pseudoconfined	2012/05/10	20:20-20:26-20:30	M1.7	N10E22	-14.5 ± 7.0	-55.5 ± 8.9	-62.4 ± 14.4
12	Pseudoconfined	2012/10/23	03:13-03:17-03:21	X1.8	S10E56	-35.2 ± 2.6	-72.3 ± 9.5	-58.1 ± 11.8
13	Pseudoconfined	2013/11/01	19:46-19:53-19:58	M6.3	S12E01	-43.4 ± 22.1	104.8 ± 11.9	114.6 ± 13.1
14	Pseudoconfined	2013/11/03	05:16-05:22-05:26	M4.9	S12W17	-139.9 ± 19.8	-71.0 ± 20.4	-65.4 ± 19.4

By carefully examining the imaging data of these confined flares, we find that three are pure-confined flares, two were accompanied by a neighboring or back-side eruption, three were associated with failed eruptions, and the other seven are pseudoconfined flares during which weak CMEs did occur. We can further find that the range of the maximum Doppler velocities of the three pure-confined flares is even smaller, from -75 to 50 km s^{-1} (the red histograms in Figures 5(a)–(c)). The above comparisons confirm the role of a CME in causing a significant Doppler velocity, and therefore suggest that the

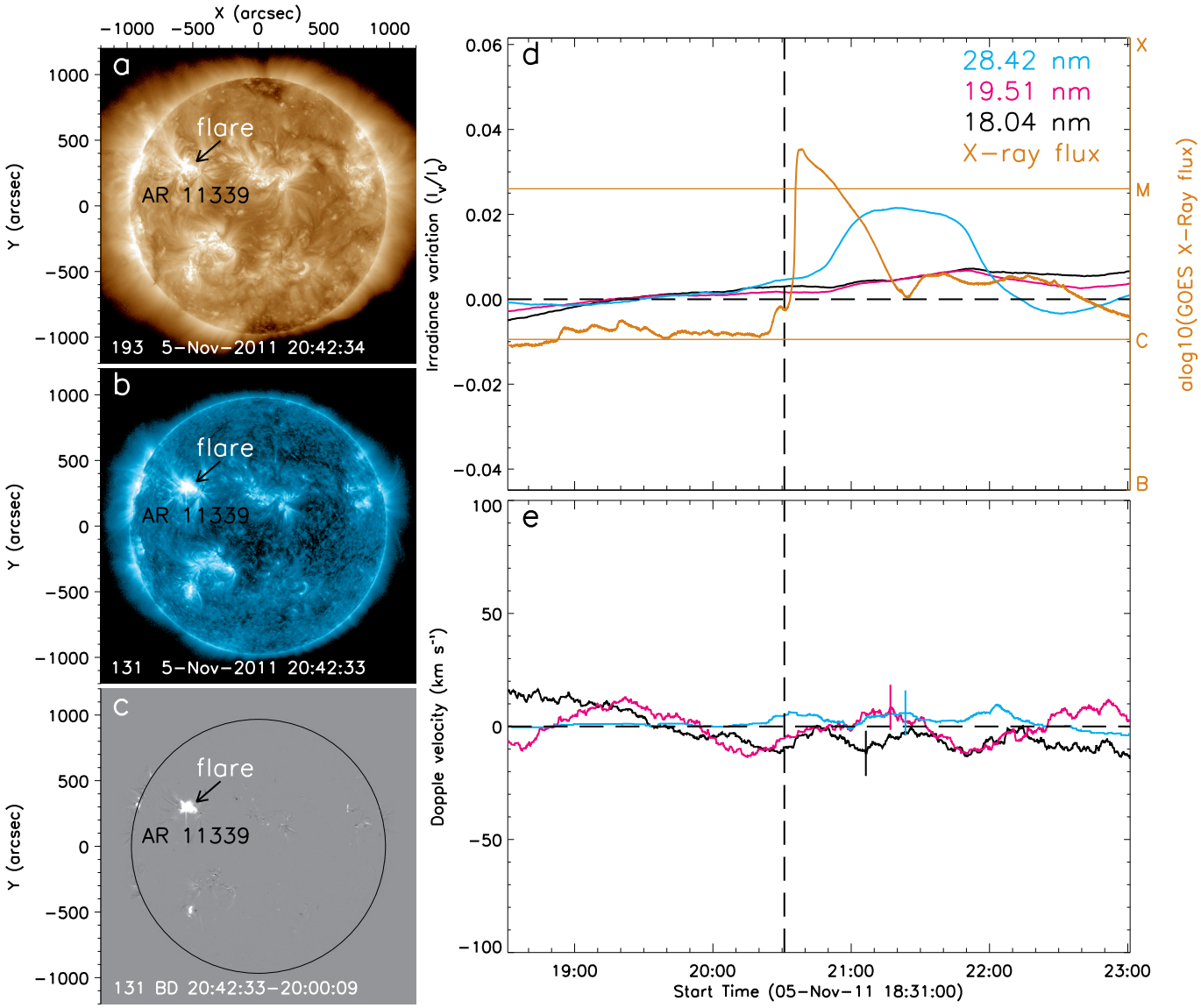

Figure 6. A compact flare without mass ejections that occurred on 2011 November 5 at 20:31 UT, exhibiting none of the corresponding Doppler response. The lack of related mass ejections is apparent in Figures 6(a) and (b), which depict direct images taken at 19.3 nm and 13.1 nm, respectively, at 20:42 UT using SDO/AIA. In Figure 6(c), a base-difference image in 13.1 nm is shown, where the preflare emission at 20:00 UT has been subtracted. Figure 6(d) portrays the Sun-as-a-star light curves obtained from SDO/EVE at three passbands, along with X-ray flux data from GOES. Notably, this compact flare is not accompanied by any significant Doppler velocities at the three target spectral lines, as illustrated in Figure 6(e). The vertical bars indicate the identified maximum Doppler velocities during the flare. The vertical dashed line in the figures indicates the start of the flare, clearly demonstrating that the compact flare, despite its occurrence, does not give rise to any related Doppler velocities at the selected spectral lines. In summary, the compact flare observed on 2011 November 5 exhibits no corresponding Doppler response, and there are no evident mass ejections associated with this event.

(An animation of this figure is available in the online article.)

Doppler responses in the selected EUV spectral lines appear to be promising signatures for identifying SMEs under the plausible assumption for solar-like stars.

3.3. Examples of Confined and Pseudoconfined Flares

The analysis of confined flares can demonstrate from another perspective the superior ability of the Doppler velocities at the selected spectral lines in discerning CMEs. The figures of all the 14 confined and pseudoconfined flares can be found at https://nadc.china-vo.org/res/r101384/ or doi:10.12149/101384. Here we present four cases.

Figure 6 demonstrates the absence of a Doppler response in a confined flare devoid of any mass ejection. This particular M1.8 class flare took place at N18°E37° in NOAA Active Region 11339, on 2011 November 5. Observations from the Atmospheric Imaging Assembly (AIA) reveal no discernible mass ejections associated with this flare, as evidenced by the lack of features in wavelengths such as 19.3 nm or 13.1 nm (Figures 6(a)–(b)). These findings persist in the base-difference image shown in Figure 6(c), which highlights any substantial changes between pre- and post-event images. Additionally, the absence of mass ejections is further supported by the lack of significant dimming in the light curves represented in Figure 6(d). Consequently, due to the lack of any observable mass ejections or related features, no Doppler response is detected for this confined flare, as depicted in Figure 6(e).

Confined flares may show a notable Doppler signature due to neighboring mass ejections, as illustrated by the event on 2011

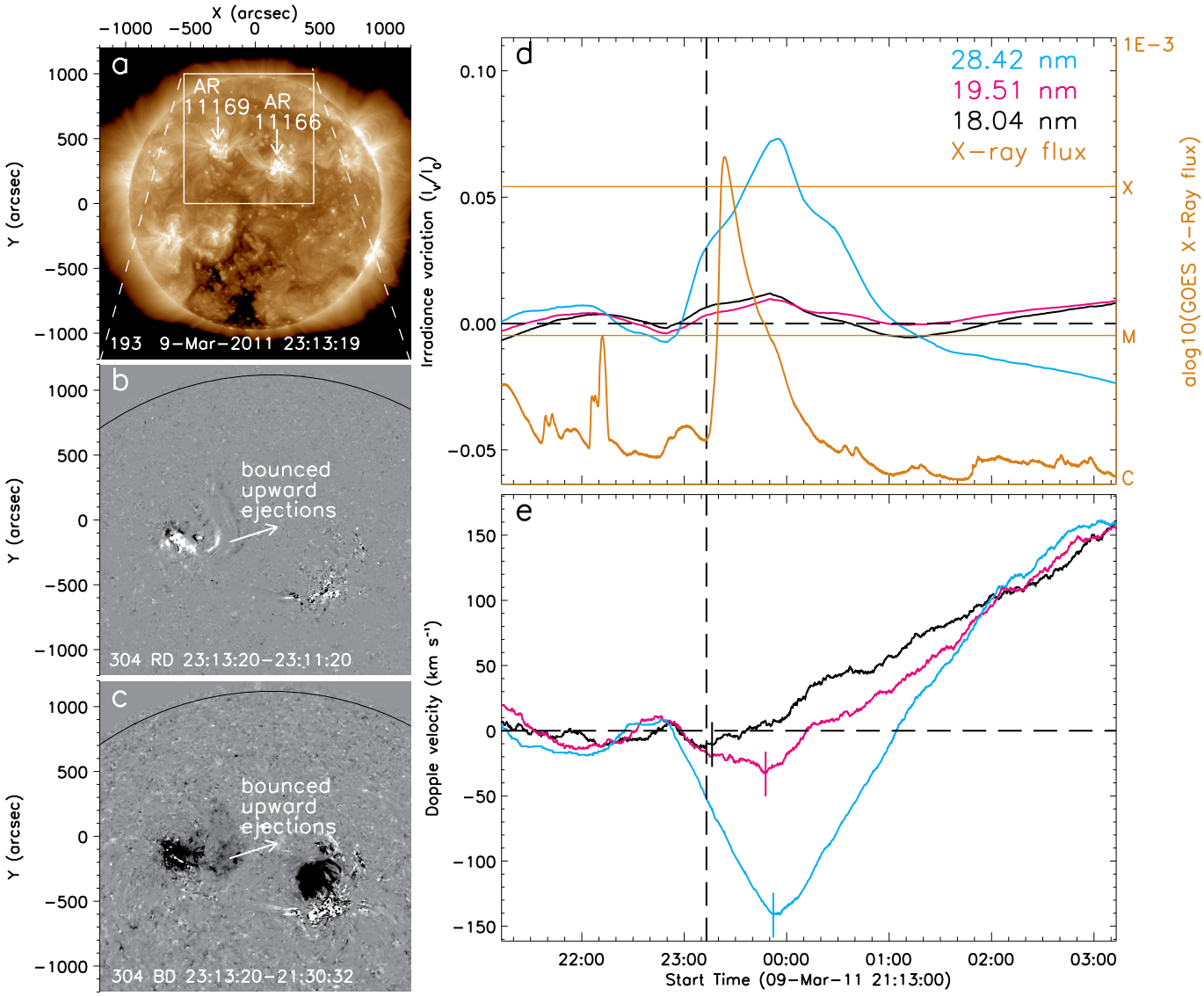

Figure 7. Doppler velocities effectively revealing the presence of mass ejections during a "confined" X1.5 flare that occurred on 2011 March 9. This flare took place in NOAA AR 11166, as depicted in Panel (a), an image captured by SDO/AIA at 19.3 nm at 23:13 UT. It was previously believed to be a confined flare without any associated mass ejections. However, the Doppler response indicates the occurrence of upward mass ejections, as indicated by the white arrows in the running-difference image shown in Panel (b) and the base-difference image in Panel (c) taken at 23:13 UT in 30.4 nm. These images are obtained by subtracting the pre-event images recorded at 23:11 UT and 21:30 UT, respectively. Panel (d) displays the light curves from SDO-EVE, along with the X-ray flux measured by GOES, providing information about the radiation emission during the X1.5 flare. The Doppler response presented in Panel (e) corresponds to the upward motion of the mass observed in Panels (b) and (c). The vertical bars indicate the identified maximum Doppler velocities associated with the upward mass ejections.

(An animation of this figure is available in the online article.)

March 9 (Figure 7). The X1.5 class flare occurring in NOAA AR 11166 at 23:13 UT was reported as a confined flare A. M. Veronig et al. (2021). Interestingly, the derived Doppler velocities increased during the flare. We closely examined the EUV observations from SDO/AIA, particularly at the 30.4 nm wavelength, and discovered the mass ejection coinciding with the X1.5 flare process. The arrows in Figures 7(b)–(c) point to the identified mass ejection. Upon conducting additional analysis, we found that the mass ejection likely originated from a preceding C9.4 flare, which peaked at 22:12 UT in the neighboring NOAA AR 11169. As the C9.4 flare-related mass ejection propagated eastward, it interacted with NOAA AR 11169 and coincidently led to the blue Doppler shifts during the X1.5 flare.

Confined flares with failed mass ejections can exhibit a weak and brief Doppler response. Figure 8 depicts two confined flares of M class that occurred on 2012 May 9, in NOAA AR 11476, both of which are associated with failed eruptions. The first flare, an M4.7 class, is characterized by ejections that propagated upward along the coronal loops in NOAA AR 11476. However, these ejections quickly returned from the loop top, as observed in Figures 8(a)–(b) (or in online movie at https://nadc.china-vo.org/res/r101384/ or doi:10.12149/101384). The second flare, an M1.8 class, led to small-scale brightening ejections, as indicated by the arrows in Figure 8(c). Additionally, there was a dimming effect where the intensity decreased by approximately 1% along the coronal loops in wavelengths of 19.51 and 18.04 nm, as shown in Figure 8(d). Analysis of the Doppler responses derived from the three EVE spectral lines (Figure 8(e)) reveals that both confined flares generated negative Doppler velocities. These velocities have values less than 30 km s^{-1} and

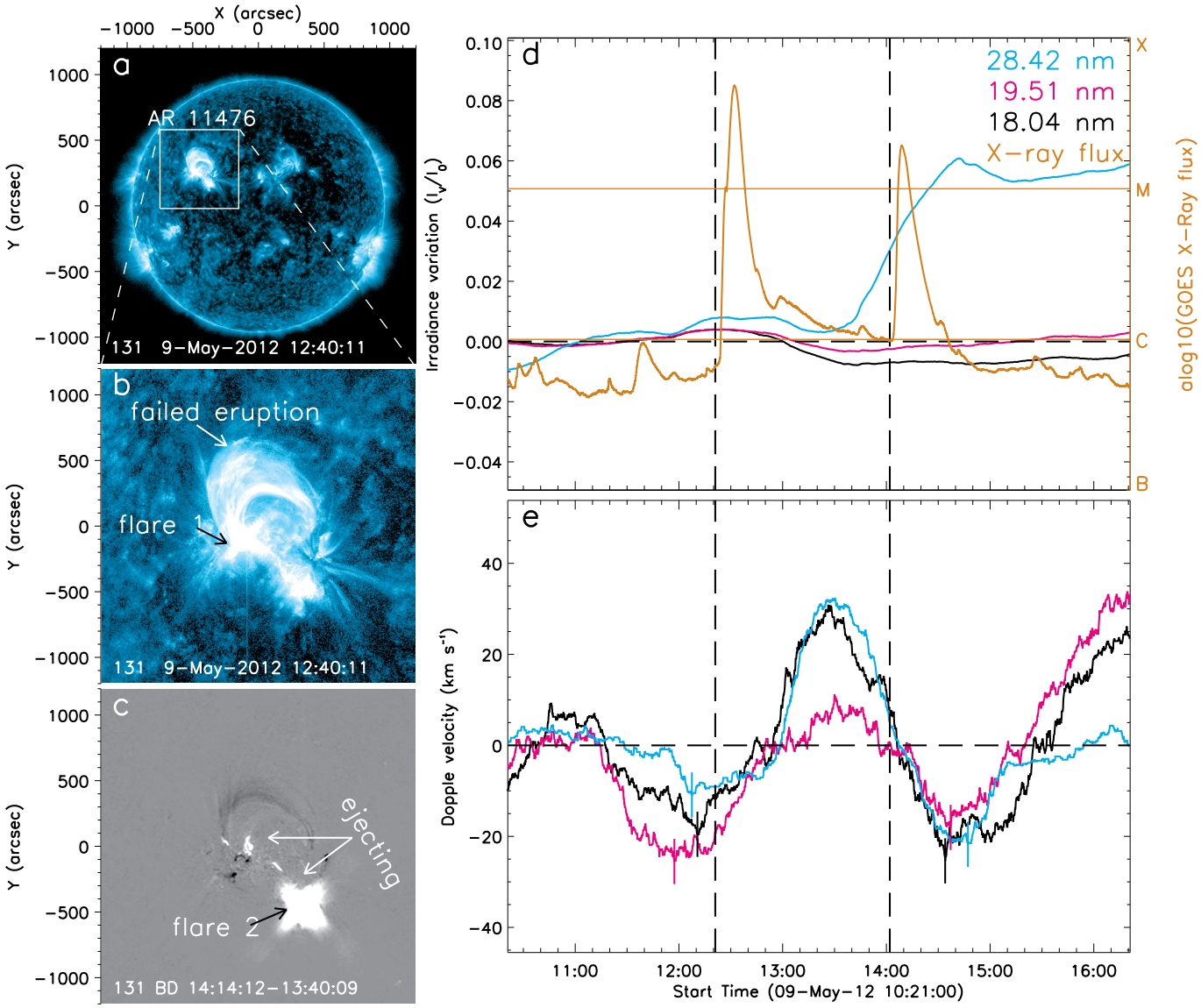

Figure 8. Two consecutive confined flares that occurred on 2012 May 9, showing the presence of subtle mass ejections, which are discerned through the detection of slow Doppler velocities of short durations. Two flares took place at different ends of a bundle of coronal loops located in NOAA AR 11476. The first flare, classified as M4.7, is depicted in Figures 8(a) and (b). Image (a) represents a snapshot in 13.1 nm taken at 12:40 UT, with the white box highlighting the region of interest. A small-scale mass ejection associated with this flare initially propagates along the coronal loop bundle in an upward direction before returning to the solar disk. The second flare, an M1.8 class, is illustrated in Figure 8(c). This base-difference image in 13.1 nm, taken at 14:14 UT, subtracts the preflare emission recorded at 13:40 UT. The mass ejections related to the M1.8 flare are observed as bright moving features, accompanied by intensity dimming along the loop bundle, indicating their ascending motion. Figure 8(d) displays the light curves obtained from SDO-EVE, along with the X-ray flux measured by GOES. These curves provide additional information about the energetic activity during the flares. In Figure 8(e), the Doppler velocities detected in these two confined flares with subtle mass ejections are presented, where the vertical bars indicate the identified maximum Doppler velocities during the flares. These Doppler velocities have short durations. Overall, the analysis reveals the presence of subtle mass ejections in these confined flares using Doppler velocities, which exhibit slow motion and short-lived characteristics. (An animation of this figure is available in the online article.)

durations of less than 1.5 hr. Notably, the Doppler responses in 19.51 nm, especially in 18.04 nm, transition from blueshifts to redshifts. This transition is consistent with the dynamic process of failed ejections, where the ascent of the ejections preceded their descent. This case further confirms that Doppler response is a sensitive indicator for identifying mass ejections.

A pseudoconfined flare is presented in Figure 9. The previously classified confined flare of X2.3 class on 2012 October 23 was actually associated with a weak CME displaying negative Doppler velocities. In EUV imaging observations (Figure 9(a)), this flare appears to be confined, lacking evident mass ejections. However, in the running-difference images (Figure 9(b)), obtained by subtracting a pre-event image taken at 03:07 UT, a faint mass can be observed propagating away from the flare region. The presence of a weak CME is further confirmed by observations from the C2 instrument on board the SOHO-LASCO, as shown in Figure 9(c). The flare/CME process, as depicted in Figure 9(d), supports the classification of this flare as a pseudoconfined event. This categorization is reinforced by the detection of negative Doppler velocities derived from EUV spectral lines at three wavelengths (Figure 9(e)).

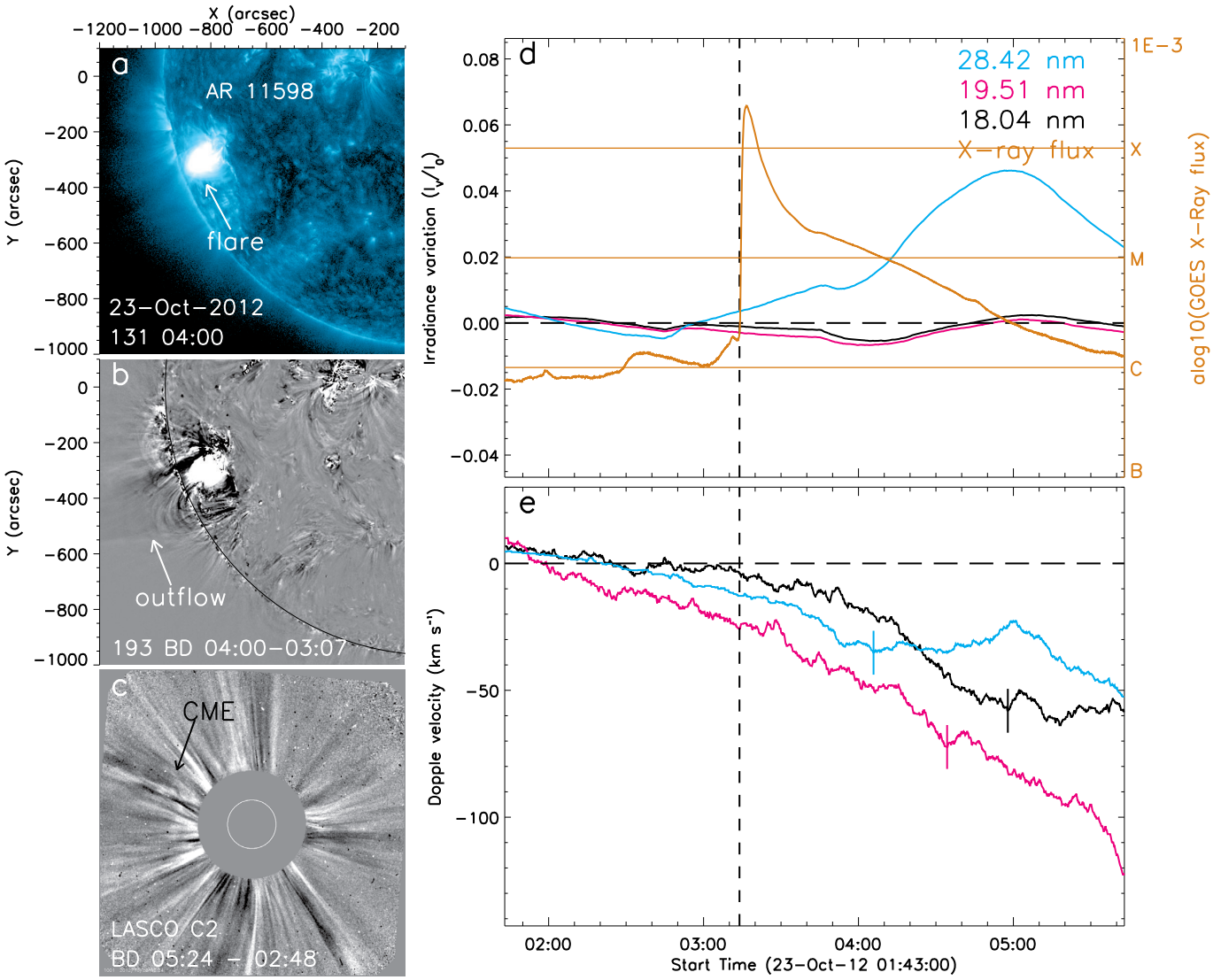

Figure 9. A pseudoconfined flare of X2.3 class on 2012 October 23, at 03:13 UT in the position of S10°E56° in NOAA AR 11598 exhibited negative Doppler velocities derived from EUV spectral lines, which was actually caused by a weak CME. Panel (a) displays an EUV image at 13.1 nm taken at 04:00 UT, capturing the flare's origin. This flare event was previously identified as a confined event in earlier research. In the base-difference image (b) at 19.3 nm, obtained by subtracting a pre-event image taken at 03:07 UT from the one at 04:00 UT, a weak dark mass can be observed propagating away from the flare region, as indicated by the white arrow. Subsequently, in the base-difference image (c) at 05:24 UT from the C2 instrument on board the SOHO-LASCO, subtracting a pre-event image at 02:48 UT, a weak CME can be discerned. Image (d) illustrates the flare/CME process using Sun-as-a-star emission data from SDO-EVE, along with X-ray flux measurements from GOES. This pseudoconfined flare was initially identified by negative Doppler velocities derived from measurements at three wavelengths using the EVE instrument (panel (e)). The vertical bars indicate the identified maximum Doppler velocities associated with the weak outflows.

(An animation of this figure is available in the online article.)

3.4. Contributors of the Doppler Signatures

A question for the Doppler responses of CMEs is why there is a large diversity in the Doppler velocity (from about −300 to 200 km s^{-1}) for these front-side CMEs (see Figures 5(a)–(c)), of which Doppler blueshifts, corresponding to negative Doppler velocities, should be expected intuitively. It is probably attributed to the mix of multiple influence factors, e.g., the motion of the flaring and dimming plasmas in the source region and the motion of the CME plasma, though the above comparative analysis has suggested that CMEs rather than flares make the major contribution to the observed Doppler responses. We investigate six factors: f_1 is the flare class, f_2 denotes flare location, f_3 means propagation direction, f_4 represents CME projection speed, f_5 is the deprojected speed, and f_6 indicates CME angular width.

The correlations between any factor and any Doppler velocity are exhibited in Figure 5(d). None of the Pearson correlation coefficients (cc) exceeds ±0.75. The strongest correlations are between flare location and the 28.42 nm Doppler velocity (cc = 0.71) and between CME propagation direction and the 28.42 nm Doppler velocity (cc = 0.67). Except for the two pairs, all the other correlations are weak with the value of cc within ±0.55. These results suggest that the Doppler response in 28.42 nm is more or less sensitive to the direction of an eruption, but for the other two lines, it seems to have a complex cause. Then we conduct the correlation analysis by using the multivariable regression method (in which all the factors are normalized into the range from 0 to 1 except the two direction factors, f_2 and f_3, in [−1, 1]) to further evaluate the contributions of these factors to the Doppler responses.

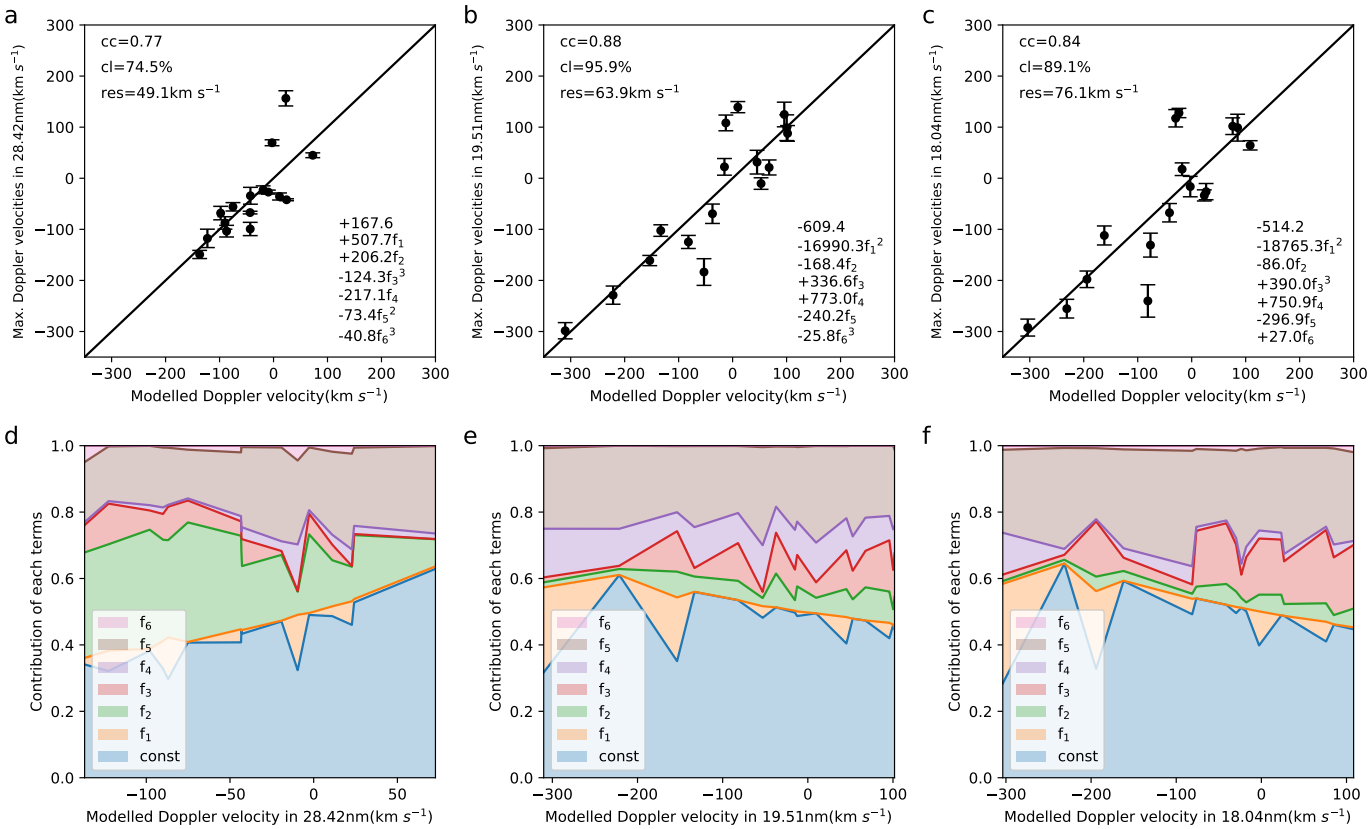

Figure 10. Correlations between the observed and modeled maximum Doppler velocities and the contributions of the factors only for the uncontaminated CME events. From the left to the right, the plots are for 28.42 nm, 19.51 nm, and 18.04 nm, respectively. The formula of the modeled Doppler velocity is given at the lower-right corner of each upper panel, and the values of the Pearson correlation coefficient (*cc*), the confidence level (*cl*), and the residual velocity (res) are denoted at the upper-left corner. The solid line is the diagonal line. In the lower panels, the normalized contributions of the terms in the modeled formulae are displayed. See Methods for the definition of the contribution.

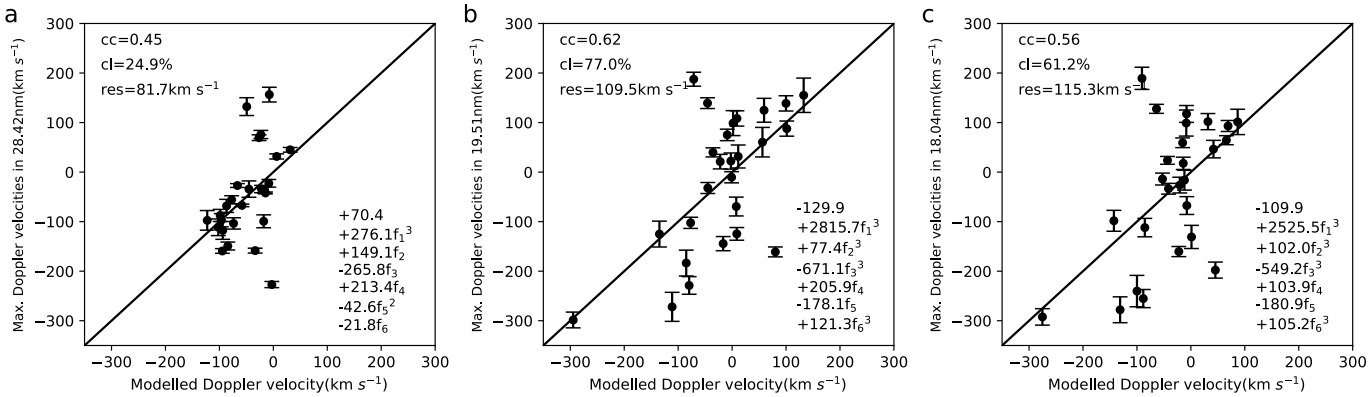

Figure 11. Correlations between the observed and modeled maximum Doppler velocities for all the 26 CME events. From the left to the right, the plots are for 28.42 nm, 19.51 nm, and 18.04 nm, respectively. The formula of the modeled Doppler velocity is given at the lower-right corner of each upper panel, and the values of the Pearson correlation coefficient, the confidence level, and the residual velocity are denoted at the upper-left corner. The solid line is the diagonal line. It could be found that the correlations become significantly worse when the contaminated events are included.

Figures 10(a)–(c) show the best fits that can be obtained between the combined factors and the Doppler velocities. For all the three lines, we can find a function from which the modeled velocities can be well correlated to the observed Doppler velocities with *cc* of 0.77, 0.88, and 0.84 and the corresponding confidence level (*cl*) of 74.5%, 95.9% and 89.1%, respectively. Especially for the lines of 19.51 and 18.04 nm, the correlation is much better than that displayed in Figure 5(d), confirming the complex cause. Further, we look closer to each term of the fitting function that roughly gives the significance of the contribution of each factor to the Doppler responses in these spectral lines, as shown in Figures 10(d)–(f). By ignoring the constant term, we may find that the flare location, f_2, and the CME deprojected speed, f_5, make the major contribution to the Doppler response in 28.42 nm. For the Doppler response in the other two lines, the largest contributor is the CME deprojected speed, while the flare location makes a much smaller contribution. In all the investigated factors, the contribution of the CME angular width, f_6, is negligible.

For completeness, we also show the multivariable regression results in Figure 11 for the sample with all the

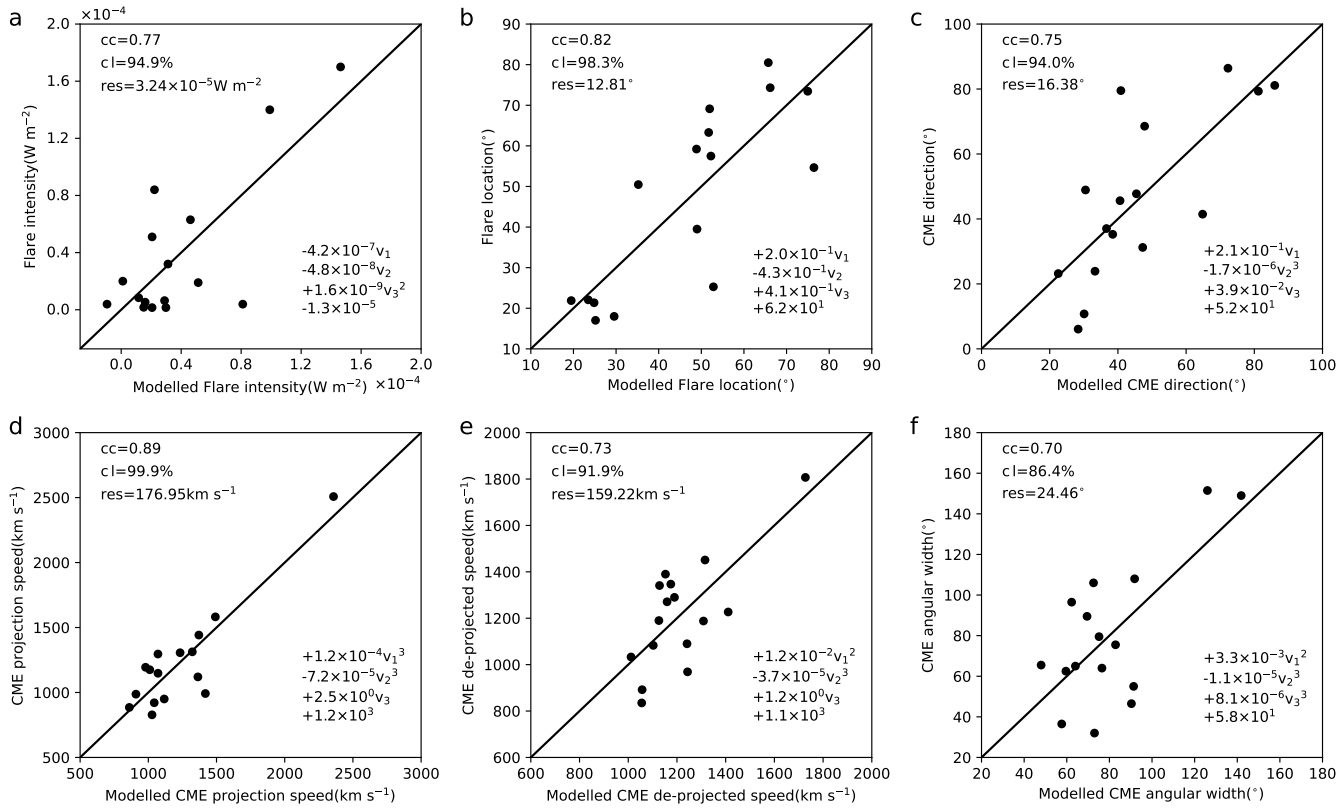

Figure 12. Correlations between the observed and modeled CME/flare properties. Similar to the upper panels in Figure 10, the model function is given at the lower-right corner of each panel, and the values of *cc*, *cl*, and res at the upper-left corner. All the velocities in the model function are in units of km s^{-1}. The high *cc* and *cl* imply that we might be able to use the remotely observable Doppler velocities to infer the nonobservable properties of the eruptions on the remote stars.

contaminated events included. The correlations become much worse. It reflects from the other side that the solar eruptive phenomena are complicated, and the relationship between the solar eruptions and Doppler velocity is hard to recover without a clear and definite sample.

3.5. Inferring CME Properties from the Doppler Velocities

It is noticed that the observed Doppler velocities are much lower than the CME propagating speeds, though the above analysis has shown the significant role of the CME speed in causing the Doppler responses. There are a couple of reasons, including the contamination from the background corona, the global averaging effect, the limited field of view of EVE, the integral effect along the line of sight, etc. Even with these limitations in observations, we still interestingly find that the combined Doppler velocities in these three lines can simulate the characteristics of CMEs and flares with the *cc* exceeding 0.70 and the *cl* above 85% or even higher, as shown in Figure 12. Here we apply a similar multivariable regression of the form $f = c_0 + \sum_{i=1}^{3} c_i v_i^{n_i}$, without normalizing the Doppler velocities because they share the same physical units. Here v_1, v_2, and v_3 are the maximum Doppler velocities in the 28.42, 19.51, and 18.04 nm lines, respectively. To assign physical meaning to the six outputs, each (otherwise dimensionless) regression factor is expressed in its native unit. For example, the factor f_1 corresponding to flare intensity is reported in W m^{-2}. For the same reasons discussed in Section 2.4, the exponents n_i are restricted to the range 0–3. The resulting relations are

$f_1 = -4.2 \times 10^{-7} v_{284} - 4.8 \times 10^{-8} v_{195} + 1.6 \times 10^{-9} v_{180}^2 - 1.3 \times 10^{-5}$ (W m^{-2}),

$f_2 = 2. \times 10^{-1} v_{284} - 4.3 \times 10^{-1} v_{195} + 4.1 \times 10^{-1} v_{180} + 6.2 \times 10^{1}$ (°),

$f_3 = 2.1 \times 10^{-1} v_{284} - 1.7 \times 10^{-6} v_{195}^3 + 3.9 \times 10^{-2} v_{180} + 5.2 \times 10^{1}$ (°),

$f_4 = 1.2 \times 10^{-4} v_{284}^3 - 7.2 \times 10^{-5} v_{195}^3 + 2.5 \times 10^{0} v_{180} + 1.2 \times 10^{3}$ (km s^{-1}),

$f_5 = 1.2 \times 10^{-2} v_{284}^2 - 3.7 \times 10^{-5} v_{195}^3 + 1.2 \times 10^{0} v_{180} + 1.1 \times 10^{3}$ (km s^{-1}),

$f_6 = 3.3 \times 10^{-3} v_{284}^2 - 1.1 \times 10^{-5} v_{195}^3 + 8.1 \times 10^{-6} v_{180}^3 + 5.8 \times 10^{1}$ (°).

It is particularly noteworthy that the remotely observed Doppler velocities in these three lines can be used to infer otherwise unobservable properties of Sun-as-a-star CMEs, including the classes (Figure 12(a)) and disk locations (Figure 12(b)) of the associated flares, the eruption directions relative to the line of sight (Figure 12(c)), the projected speeds (Figure 12(d)) and deprojected speeds (Figure 12(e)), as well the angular widths (Figure 12(f)).

4. Discussions and Conclusion

Using continuous MEGS-A observations from SDO/EVE, we conducted an analysis on over a dozen spectral lines spanning low- to high-temperature formation. This analysis aimed to identify which lines are most effective for Sun-as-a-star detection of CME features. We performed a statistical study of all fast, well-defined front-side CMEs in 2012 with projected speeds $\geqslant$800 km s^{-1} under sufficient observational coverage. Three main results emerge. (1) After excluding contaminated ("dirty") lines, Doppler shift diagnostics show that not all lines are suitable for CME detection. Among the

SDO/EVE lines, we identify three (18.4, 19.3, and 28.4 nm) that reliably capture CME features. With these lines, eruptive events display consistently longer and stronger Doppler responses than confined events of comparable flare class. (2) Because full-disk measurements average over the solar disk, the measured Doppler velocities represent only a fraction of the true CME/SME speeds. Guided by forward simulations, we derive, for each line, an empirical relation linking Sun-as-a-star Doppler velocities to the underlying ejection speeds. (3) With a multivariable regression approach, six CME properties—the related flare class, flare disk location, eruption direction relative to the line of sight, projected and deprojected speeds, and angular widths—can be estimated from Sun-as-a-star Doppler velocities measured in the 28.42, 19.51, and 18.04 nm lines.

It is essential to exercise caution in line selection because CME signals are often blended with dynamics from the associated flare. Our aim is to identify spectral lines that can distinguish Sun-as-a-star CME signatures from flare signatures. A CME typically perturbs multiple atmospheric layers from the photosphere and chromosphere through the transition region to the high corona and involves multicomponent eruptions with characteristic temperatures ranging from chromospheric/prominence material below 10^4 K, to transition-region plasma at 10^4–10^5 K, and up to several MK coronal plasma. In most cases, especially for fast events, CMEs are accompanied by flares (e.g., G. Zhou et al. 2003). Flare processes may include chromospheric evaporation, coronal rain condensation, chromospheric compression, and other chromospheric activity (e.g., Z. Cheng et al. 2019). Characteristic CME features are often linked to the successful eruption of filaments (e.g., Y. Xu et al. 2022) or of magnetic flux ropes, the latter commonly reaching temperatures up to ∼10 MK (J. Zhang et al. 2012) and propagating from the low corona into interplanetary space. The interplanetary counterpart of CME-related flux ropes was detected in situ as early as L. Burlaga et al. (1981). In the classic three-part CME, the bright core corresponds to the erupting prominence (typical temperature $\sim 10^4$ K), while the dark cavity is generally interpreted as the flux rope. A key open question is whether a CME-related filament can travel to large distances without substantial heating and diffusion. Accordingly, particular care should be taken when selecting lower-temperature lines for Sun-as-a-star CME detection until they are validated as faithfully capturing the CME Doppler responses.

As a consistency check, we applied the same derivation method to MEGS-B observations of the 2012 July 12 event and obtained Sun-as-a-star Doppler velocities in He I 58.43 nm, O V 62.96 nm, and O VI 103.1 nm, as shown in Figure 13. In contrast to the negative Doppler velocities (blueshifts) derived from MEGS-A (Fe XI 18.04 nm, Fe XII 19.51 nm, and Fe XV 28.42 nm), the MEGS-B lines yield positive Doppler velocities (redshifts). Using the same procedure, we also examined the 2021 October 28 event with MEGS-B lines Ne VII 46.52 nm, O III 52.57 nm, and O V 62.96 nm as in Y. Xu et al. (2022), and found a similar short-lived maximum velocity of about (−400 km s^{-1}) lasting less than 10 minutes. These Doppler blueshifts persist for a much shorter time than the GOES soft X-ray irradiance enhancement. Y. Xu et al. (2022) attributed such velocities to "secondary components" caused by a mass ejection during the impulsive phase and shortly after the flare peak, and T. Otsu & A. Asai (2024) likewise reported Sun-as-a-star filament eruption speeds of ∼400 km s^{-1} over similarly brief intervals. According to Large Angle and Spectrometric Coronagraph (LASCO) measurements[1], the related CMEs in Y. Xu et al. (2022) and T. Otsu & A. Asai (2024) reached linear projected speeds of 1519 km s^{-1} and 1222 km s^{-1}, respectively. Thus, a maximum Sun-as-a-star Doppler velocity of ∼−400 km s^{-1} may plausibly reflect the underlying CME speed once global disk-integration effects are considered, as discussed here. The remaining inconsistencies across events underscore the need to enlarge the sample to evaluate the robustness of lower-temperature lines for Sun-as-a-star CME detection.

The data quality requirements, relevant timescales, detection thresholds, and instrumental characteristics for EUV spectroscopic detection of SMEs have been discussed and simulated by Z. H. Yang et al. (2022, 2024). Z. H. Yang et al. (2022) used analytic modeling and spectral synthesis to provide the first systematic demonstration that CMEs can be detected from asymmetries in Sun-as-a-star EUV-line profiles, proposing key instrument constraints: signal-to-noise ratio ($S/N \geqslant 100$) and spectral resolving power ($R \geqslant 500$). They also highlighted line-blending challenges in practice; for instance, the blue wing of Fe XII 19.51 nm can be contaminated by Fe VIII 19.47 nm and by unidentified lines. Moreover, fast CMEs (>500 km s^{-1}) are more prone to blending, while slowly accelerating CMEs require higher ($S/N \approx 100$–150) at the same resolution. These theoretical studies, however, do not fully capture the complex physics of CME evolution (e.g., mass loading and multithermal structuring). In follow-up work, Z. H. Yang et al. (2024) further developed an analytic framework for G-type stars, showing that a medium-resolution EUV spectrograph ($R \approx 500$, $S/N \approx 30$) can detect Earth-directed CMEs and achieve velocity accuracies better than ±30%. They recommend focusing on late-eruption phases and prioritizing short-wavelength EUV lines with lower interstellar absorption (e.g., Fe IX λ 171), while balancing resolution and sensitivity. These results offer valuable guidance for EUV spectroscopic SME detection, but their efficacy must be verified, expanded, and refined using analyses of stellar flare observations and associated phenomena.

Another key aspect of this work involves inferring Sun-as-a-star CME properties from modeled Doppler velocities in three EUV lines—28.42, 19.51, and 18.04 nm—using a multivariable regression. The six inferred parameters include the associated flare class and disk location, the eruption direction relative to the line of sight, the projected and deprojected speeds, and the angular width. These relationships with Doppler velocities are derived from carefully simulated, uncontaminated Sun-as-a-star CMEs, accounting for global disk-integration effects. These results offer a promising pathway for studying remote SMEs. However, our extrapolation to stellar data relies on several key assumptions: (1) Solar-like stars (G/K dwarfs) are expected to share broadly similar CME and flaring geometries, as well as coronal thermodynamics, at the temperatures sampled by the three selected EUV lines. (2) The three EUV lines (28.42, 19.51, and 18.04 nm) exhibit comparable formation behaviors in solar-like corona, making them suitable for analogous studies of stellar corona. (3) The dilution/projection effects that influence Sun-as-a-star Doppler amplitudes are expected to apply similarly to unresolved stellar observations. (4) Limited stellar context (such as flare energy class proxies, rotational and active-region indicators) can supply weak priors to help

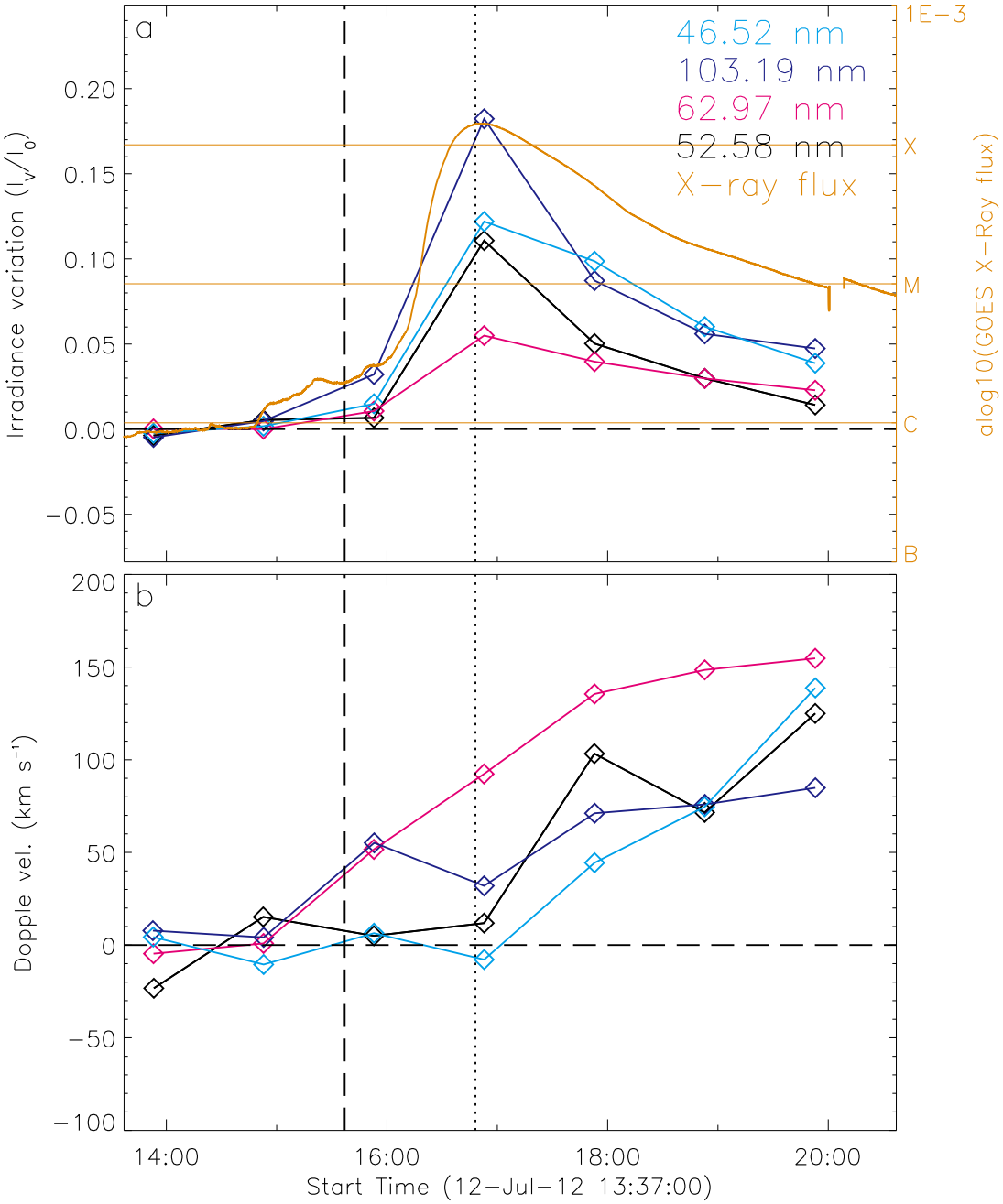

Figure 13. For the CME on 2012 July 12, Sun-as-a-star Doppler velocities derived from SDO/EVE showing positive shifts (redshifts) in four passbands: He I 58.43 nm (black color), O V 62.96 nm (purple color), O VI 103.1 nm (blue color), and 46.52 nm (cyan). At each time step, the irradiance is normalized by the 2 hr pre-eruption average; the horizontal dashed line marks 0% relative change. From the EVE line profiles, redshifted Doppler velocities are obtained in all four passbands; vertical bars denote the identified maximum Doppler velocities associated with the CME. The vertical dashed line indicates the flare onset, and the vertical dotted line marks the CME's first appearance in LASCO/C2.

constrain the geometry when interpreting line-of-sight velocities in stellar data. Despite these assumptions, further work is required to refine the application of the Sun-as-a-star EUV-line approach for stellar CME detection. In particular, future efforts should focus on quantifying how SME parameters in stellar environments (such as flare class, SME speed, and angular width) relate to Doppler velocities inferred from various spectral lines. This should be achieved through combined observations and simulations to better understand how to apply solar scaling laws to stellar observations with lower S/N.

In summary, we conducted a proof-of-concept Sun-as-a-star experiment to detect SMEs using solar CMEs as a proxies, analyzing EUV spectral lines from EVE on board the SDO. By comparing 26 front-side fast CMEs with 14 confined M1.0-plus flares, we discover that the Doppler responses in 18.04, 19.51, and 28.42 nm during CME events provide a

promising diagnostic to distinguish Sun-as-a-star CME signals from flare signals. We further show that CME characteristics can be reasonably reproduced from the Doppler velocities in these three lines, offering a promising way to infer otherwise unobservable properties of eruptions on distant stars. Considering the multiline response to the complex CME dynamics, we finally recommend three EUV lines, 18.4, 19.3, and 28.4 nm, as the preferred choices for detecting Sun-as-a-star CME signatures.

Our statistical analysis underscores the complexity of using Doppler responses in spectral lines to detect SMEs: not every line is suitable for identifying Sun-as-a-star CMEs. Accurate SME detection is crucial for understanding stellar evolution and activity and for the search for habitable stellar systems and extraterrestrial life. Broader comparative studies—across additional spectral lines and target stars—are needed to clarify the mapping between Doppler response and SME activity. It is worth emphasizing that EUV spectra of extrasolar stars were obtained exclusively by the Extreme Ultraviolet Explorer (S. Bowyer & R. F. Malina 1991) from 1992 June 7 to 2001 January 31; more than two decades have now passed since those observations. Building upon the present results and recent technological advances, we advocate a revival of EUV stellar spectroscopy, as exemplified by initiatives such as the Extreme-ultraviolet Stellar Characterization for Atmospheric Physics and Evolution (ESCAPE; K. France et al. 2019).

This work not only clarifies the challenges and limitations of detecting SMEs from Doppler signatures but also outlines a practical strategy for selecting suitable spectral lines. By statistically analyzing a substantial sample of CMEs and confined events in Sun-as-a-star observations, we establish a robust foundation for future studies of SMEs on other stars.

Supplementary materials: (1) The plots of all the other 25 CME events. (2) The plots of 14 confined flares. (3) The temperature response profiles of 13 spectral lines from the EVE MEGS-A channel. (4) Five animations corresponding to Figure 4 and Figures 6–9.

Acknowledgments

We thank the anonymous referee for the insightful comments and constructive suggestions that substantially improved the clarity and quality of this manuscript. G.P.Z. is grateful to Prof. J. Lin and Dr. Z. J. Zhou for their helpful discussions and kind assistance with improving the figures. We acknowledge use of the EVE and AIA data from the SDO spacecraft, and the coronagraph images from STEREO-A and B and SOHO missions. The work is supported by the National Key R&D Program of China (2022YFF0503800), the Strategic Priority Research Program of the Chinese Academy of Sciences (XDB0560000), the State Key Program of National Natural Science Foundation of China (grant No. 12533010), and the National Natural Science Foundation of China (12403067, 12350004, 12373111, 12273061, 12273060). The authors from the University of Science and Technology of China are also supported by the National Natural Science Foundation of China (42188101) and the Innovation Program for Quantum Science and Technology (2021ZD0300302). Y.W. is particularly grateful for the support of the New Cornerstone Science Foundation through the Xplorer prize.

Data Availability

The SDO data used in this paper can be downloaded from http://jsoc.stanford.edu/. The LASCO data can be downloaded from https://soho.nascom.nasa.gov/data/data.html. The STEREO-A/B COR2 data can be retrieved from http://sd-www.jhuapl.edu/secchi/lz/L0/.

Code Availability

The data analysis was done with SolarSoft packages[10] in the Interactive Data Language. The spectral inversion code is available upon request from the authors.

ORCID iDs

Zhixun Cheng https://orcid.org/0000-0002-4020-3211
Anchuan Song https://orcid.org/0000-0002-3237-3819
Guiping Zhou https://orcid.org/0000-0001-8228-565X
Yuming Wang https://orcid.org/0000-0002-8887-3919
Hui Tian https://orcid.org/0000-0002-1369-1758
Xiaolei Li https://orcid.org/0000-0002-7685-1528
Jifeng Liu https://orcid.org/0000-0002-2874-2706
Jingxiu Wang https://orcid.org/0000-0003-2544-9544

References

Aarnio, A. N., Matt, S. P., & Stassun, K. G. 2012, ApJ, 760, 1, 9
Argiroffi, C., Reale, F., Drake, J. J., et al. 2019, NatAs, 3, 742
Burlaga, L., Sittler, E., Mariani, F., & Schwenn, A. R. 1981, JGRA, 86, 6673
Bowyer, S., & Malina, R. F. 1991, AdSpR, 11, 205
Cheng, Z., Wang, Y., Liu, R., Zhou, Z., & Liu, K. 2019, ApJ, 875, 93
Dere, K. P., Landi, E., Mason, H. E., Fossi, B. M., & Young, P. R. 1997, A&AS, 125, 149
Dere, K. P., Landi, E., Young, P. R., et al. 2009, A&A, 498, 915
Drake, J. J., Cohen, O., Yashiro, S., & Gopalswamy, N. 2013, ApJ, 764, 170
Eddy, J. A. 1979, A New Sun: The Solar Results from Skylab (NASA)
Feynman, J., & Hundhausen, A. J. 1994, JGR, 99, 8451
France, K., Fleming, B. T., Drake, J. J., et al. 2019, SPIE, 11118, 38
Gallagher, P. T., Lawrence, G. R., & Dennis, B. R. 2003, ApJ, 588, 53
Green, L.M., Matthews, S. A., van DrielYGesztelyi, L., Harra, L. K., & Culhane, J. L. 2002, SoPh, 205, 325
Guenther, E. W., & Emerson, J. P. 1997, A&A, 321, 803
Houdebine, E. R., Foing, B. H., & Rodono, M. 1990, A&A, 238, 249
Leitzinger, M., Odert, P., & Greimel, R. 2024, MNRAS, 532, 1486
Leitzinger, M., Odert, P., Ribas, I., et al. 2011, A&A, 536, A62
Mishra, W., Srivastava, N., Wang, Y., et al. 2019, MNRAS, 486, 4671
Namekata, K., Airapetian, V. S., Petit, P., et al. 2024, ApJ, 961, 23
Namekata, K., Maehara, H., Honda, S., et al. 2022, NatAs, 6, 241
Odert, P., Leitzinger, M., Hanslmeier, A., & Lammer, H. 2017, MNRAS, 472, 876
Osten, R. A., & Wolk, S. J. 2015, ApJ, 809, 79
Otsu, T., & Asai, A. 2024, ApJ, 964, 75
Pesnell, W. D., Thompson, B. J., & Chamberlin, P. C. 2012, The Solar Dynamics Observatory (SDO) (Springer), 3
Qiu, J., Wang, H., Cheng, C., & Gary, D. E. 2004, ApJ, 604, 900
Svestka, Z., & Cliver, E. W. 1992, in Lecture Notes in Physics, ed. Z. Svestka, B. V. Jackson, & M. Machado, Vol. 399 (Springer), 1
Thernisien, A. 2011, ApJS, 194, 33
Thernisien, A. F. R., Howard, R. A., & Vourlidas, A. 2006, ApJ, 652, 763
Veronig, A. M., Odert, P., Leitzinger, M., et al. 2021, NatAs, 5, 697
Wang, Y., Zhou, Z., Zhang, J., et al. 2016, ApJS, 223, 4
Wang, Y. M., Ye, P. Z., Wang, S., Zhou, G. P., & Wang, J. X. 2002, JGRA, 107, A11, 1340, SSH-2
Woods, T. N., Eparvier, F. G., Hock, R., et al. 2012, SoPh, 275, 115
Xu, Y., Tian, H., Hou, Z., et al. 2022, ApJ, 931, 76
Yang, Z. H., Tian, H., Bai, X. Y., et al. 2022, ApJS, 260, 36
Yang, Z. H., Tian, H., Zhu, Y. J., et al. 2024, ApJ, 966, 24
Zhang, J., Cheng, X., & Ding, M. 2012, NatCo, 3, 747
Zhang, J., Dere, K. P., Howard, R. A., et al. 2001, ApJ, 559, 452
Zhou, G., Wang, J., & Cao, Z. 2003, A&A, 397, 1057

[10] https://www.lmsal.com/solarsoft/